FERMILAB-PUB-25-0379-SQMS

Ultracoherent superconducting cavity-based multiqudit platform with error-resilient control

Taeyoon Kim,[1,2,*] Tanay Roy,[1,*] Xinyuan You,[1] Andy C. Y. Li,[1] Henry Lamm,[1] Oleg Pronitchev,[1] Mustafa Bal,[1] Sabrina Garattoni,[1] Francesco Crisa,[1] Daniel Bafia,[1] Doga Kurkcuoglu,[1] Roman Pilipenko,[1] Paul Heidler,[1] Nicholas Bornman,[1] David van Zanten,[1] Silvia Zorzetti,[1] Roni Harnik,[1] Akshay Murthy,[1] Shaojiang Zhu,[1] Changqing Wang,[1] André Vallières,[1] Ziwen Huang,[1] Jens Koch,[2] Anna Grassellino,[1] Srivatsan Chakram,[3,†] Alexander Romanenko,[1,‡] and Yao Lu[1,§]

[1] *Superconducting Quantum Materials and Systems (SQMS) Center, Fermi National Accelerator Laboratory, Batavia, IL 60510, USA*
[2] *Department of Physics and Astronomy, Northwestern University, Evanston, Illinois 60208, USA*
[3] *Department of Physics and Astronomy, Rutgers University, Piscataway, NJ 08854, USA*

(Dated: June 5, 2025)

Superconducting radio-frequency (SRF) cavities offer a promising platform for quantum computing due to their long coherence times and large accessible Hilbert spaces, yet integrating nonlinear elements like transmons for control often introduces additional loss. We report a multimode quantum system based on a 2-cell elliptical shaped SRF cavity, comprising two cavity modes weakly coupled to an ancillary transmon circuit, designed to preserve coherence while enabling efficient control of the cavity modes. We mitigate the detrimental effects of the transmon decoherence through careful design optimization that reduces transmon-cavity couplings and participation in the dielectric substrate and lossy interfaces, to achieve single-photon lifetimes of 20.6 ms and 15.6 ms for the two modes, and a pure dephasing time exceeding 40 ms. This marks an order-of-magnitude improvement over prior 3D multimode memories. Leveraging sideband interactions and novel error-resilient protocols, including measurement-based correction and post-selection, we achieve high-fidelity control over quantum states. This enables the preparation of Fock states up to $N = 20$ with fidelities exceeding 95%, the highest reported to date to the authors' knowledge, as well as two-mode entanglement with coherence-limited fidelities reaching up to 99.9% after post-selection. These results establish our platform as a robust foundation for quantum information processing, allowing for future extensions to high-dimensional qudit encodings.

I. INTRODUCTION

Bosonic quantum systems have emerged as a compelling platform for quantum computing, offering several intrinsic advantages over traditional qubit-based architectures. By encoding quantum information in harmonic oscillator modes, these systems benefit from long coherence times, large Hilbert spaces, and relatively simple error channels dominated by photon loss. Coupling to nonlinear superconducting circuits has enabled universal control and gate operations using a variety of techniques [1–7] in both single-mode [8] and multimode [9, 10] circuit QED systems implemented with three-dimensional (3D) microwave cavities featuring millisecond-scale coherence times. These capabilities have enabled hardware-efficient implementations of bosonic quantum error correction, including demonstrations that surpass the break-even point [11–13]. More recently, these control strategies have begun to extend to ultra-high-coherence cavities [14, 15], with coherence times exceeding tens of milliseconds and the potential for further improvements [16], opening new avenues for scalable quantum information processing.

Qubit-based quantum computing has long been the dominant paradigm, and even in bosonic error correction, cavity modes are typically used to encode logical qubits [17, 18]. However, the large Hilbert space of a cavity also makes it a natural platform for implementing qudits, both natively and with error correction [19]. Qudits offer enhanced information density and can enable more compact and efficient quantum circuits across a wide range of algorithms [20–22]. They are particularly well-suited for quantum simulations in chemistry [23, 24], condensed matter [25], and high-energy physics (HEP), where they can naturally represent physical degrees of freedom such as large spins, rotors, and gauge fields [26]. In HEP applications, for instance, a quantum field can be discretized in position space and encoded within a single high-dimensional qudit [27]. The advent of ultrahigh-coherence cavities makes qudit-based computation and simulation increasingly viable, enabling high-fidelity control over progressively higher Fock states and paving the way for qudit-based quantum processors and simulators.

Despite their advantages, ultrahigh-coherence cavities pose increasing challenges for quantum control as coherence times improve. A central tension arises between achieving fast, high-fidelity control and preserving the cavity's exceptional coherence. Strong coupling to ancillary transmon circuits enables fast gates but introduces

* Equal contribution
† schakram@physics.rutgers.edu
‡ aroman@fnal.gov
§ yaolu@fnal.gov

photon loss through the inverse Purcell effect and exposes the cavity to backaction from ancilla errors. On the other hand, weak coupling preserves coherence but slows down gates and increases susceptibility to ancilla decoherence during the operation. This trade-off can be mitigated by driving the cavity or ancilla to achieve gate speeds exceeding the native interaction rate, using techniques such as conditional displacements [2], sideband interactions [28], and sideband-enhanced selective number-dependent arbitrary phase (SNAP) gates [29]. Nevertheless, as coherence continues to improve, it becomes increasingly important to develop control strategies that are not only fast, but also fault-tolerant and compatible with the demands of even higher coherence platforms [30].

In this work, we present a two-mode bosonic quantum system implemented within a multimode superconducting radio-frequency (SRF) cavity, achieving ultrahigh coherence times and novel cavity control capabilities resilient to ancilla errors. Our system utilizes a two-cell SRF cavity designed based on the TESLA geometry, weakly coupled to a transmon circuit for precise quantum control while preserving cavity coherence. We achieve single-photon lifetimes of 20 ms and 16 ms for the two bosonic modes, significantly longer than most state-of-the-art cavity QED platforms, establishing a record for multimode quantum memories. Despite the coherence-preserving weak coupling, we employ sideband operations to achieve fast cavity control on timescales far shorter than those set by the weak dispersive shift. In conjunction with novel protocols that make cavity control leading-order immune to ancilla errors, we achieve high-fidelity preparation of Fock states up to $N = 20$ with fidelity exceeding 95%, as well as two-mode entanglement with coherence-limited fidelities achievable up to 99.9% after post-selection. These advancements in coherence and control mark a significant step in bosonic quantum computing, opening avenues for exploring high-dimensional qudit encodings and gate operations.

II. CAVITY CHARACTERIZATION AND SYSTEM DESIGN

We designed a two-mode superconducting cavity based on the multi-cell TESLA geometry [31, 32], consisting of two elliptically shaped cells connected by a circular aperture referred to as the iris, as shown in Fig. 1(a). The cavity supports two normal modes, named "Alice" and "Bob", which arise from the hybridization of the nearly degenerate bare TM_{010} modes, resulting in symmetric and antisymmetric electric field profiles, respectively (Fig. 1(b)). The radius of the iris controls the coupling strength and consequently the frequency detuning between the modes. The Alice and Bob modes are designed to have frequencies of 5.779 GHz and 6.872 GHz, respectively, allowing for the integration of a transmon qubit that couples to both modes simultaneously. Cylin-

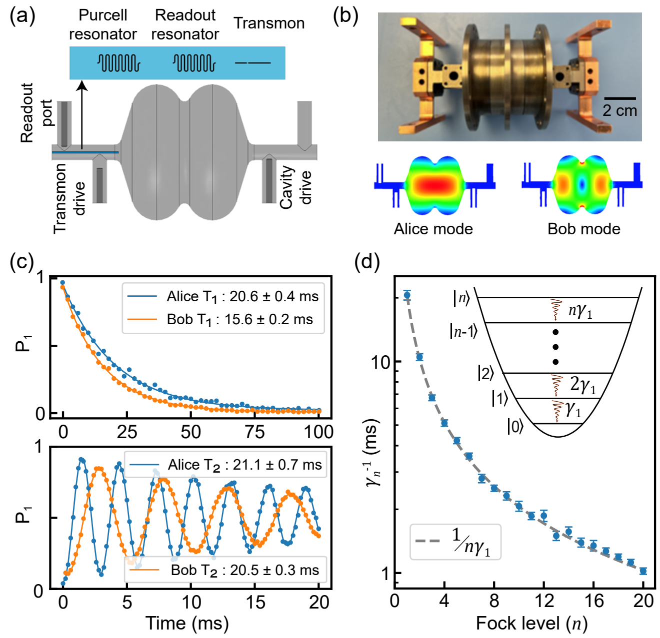

FIG. 1. **Device architecture and coherence properties.** **(a)** Schematic of the double-cell elliptical SRF cavity with four ports for RF control. Three ports are used in this experiment. The chip (blue) contains an ancilla transmon, a Purcell filter and a half-wave strip-line resonator for measuring the transmon. **(b)** Picture of the Niobium cavity (top panel) with mounting brackets made of OFC copper. Bottom panel shows the electric field distribution of the two fundamental modes dubbed 'Alice' and 'Bob'. **(c)** Coherence times of the single photon states obtained using T_1 and Ramsey experiments. **(d)** Relaxation times of Alice mode's Fock levels up to $|20\rangle$ with a fit to $1/(n\gamma_1)$, where n is the Fock state photon number and $\gamma_1 = 1/T_1^{(1)}$ is the decay rate of $|1\rangle$. The inset shows that the theoretical decay rate of Fock $|n\rangle$ is equal to $n\gamma_1$ for a harmonic oscillator.

drical waveguide pipes with sufficiently high cut-off frequencies (35 GHz) are attached on either side of the cavity; one of these houses the transmon. Additionally, each pipe includes two ports for microwave drive lines to control various components.

We manufactured this cavity from high-purity niobium, using e-beam welding to eliminate seam loss. State-of-the-art surface treatments, such as chemical etching and heat treatments, were applied to remove damaged surface layers and contaminants. These steps enable high quality factors for the cavity modes at milli-Kelvin in the low-photon regime [14–16, 33], providing an excellent platform for quantum computing applications.

To establish a baseline for the cavity's performance before integrating the transmon qubit, we first characterized the bare cavity at 8 mK in a dilution refrigerator. Using a classical decay measurement, we confirmed that the two fundamental modes exhibit exceptionally long decay times of 25.5 ms and 19.3 ms, respectively, corresponding to loaded quality factors of about 9.4×10^8

and 8.4×10^8. To maintain this high-Q, we keep the probe antenna highly undercoupled ($Q_{\text{ext}} > 10^{11}$), thus preventing external losses from limiting the cavity lifetime. We also performed temperature-dependent measurements of the cavity's decay times to distinguish residual resistance from two-level-system (TLS) contributions, obtaining results comparable with established SRF best practices (see Appendix B). These findings confirm the suitability of this design for quantum memory applications and demonstrate that our fabrication and preparation steps effectively preserve the cavity's coherence, laying the groundwork for subsequent transmon integration.

To achieve universal control of the two-mode cavity as a quantum processing unit (QPU), we introduce a transmon qubit that simultaneously couples to the two normal modes, thanks to their similar electric field strengths at the opening of the transmon tunnel. This integration requires careful optimization since the transmon can introduce the inverse Purcell effect and other loss mechanisms to the cavity [14]. We adopt two main strategies for this optimization. First, we carefully engineer the cavity geometry to minimize the transmon chip's participation in the cavity field. Second, we reduce the dispersive shift by adjusting the transmon's location along the axis of the cavity, further lowering its participation ratio while maintaining sufficient coupling for cavity control (see Appendix C for details). RF simulations confirm that these modifications preserve the TESLA geometry's inherent low-loss advantage, enabling robust two-mode control with the ancilla qubit without sacrificing the cavity's long coherence times.

In our experiment, a transmon with frequency $\omega_q/2\pi = 6.402\,\text{GHz}$, relaxation time of $T_1^{ge} = 147.4\ \mu\text{s}$ and Ramsey decay times of $T_2^{ge} = 47.3\ \mu\text{s}$ is integrated with the 2-cell cavity for control and readout. The coupling to the modes is adjusted to obtain similar weak dispersive shifts ($\chi_e/2\pi$) of −71 kHz for Alice and −96 kHz for Bob. We measure the single-photon lifetime $T_1^{(1)} = 1/\gamma_1$ of 20.6 ms for Alice and 15.6 ms for Bob modes, which are reasonably close to the baseline cavity lifetimes. We also measure the T_2 of the modes by preparing a $|0\rangle$ and $|1\rangle$ superposition state, finding 21.1 ms and 20.5 ms for Alice and Bob modes, respectively. From these measurements, we extract a pure dephasing time of around 43 ms and 60 ms for the two modes, which can be accounted for by the transmon's thermal shot noise (see Appendix A).

A characteristic property of a linear system is that the decay rate of a Fock state γ_n is proportional to its photon number, i.e. $\gamma_n = n\gamma_1$. Equivalently, the lifetime of the n-th Fock state satisfies $\text{T}_1^{(n)} = \text{T}_1^{(1)}/n$. We experimentally verify this relationship by preparing Fock states with increasing photon numbers (as described in the next section) and measuring their relaxation times. Figure 1(d) shows the measured data in excellent agreement with the theoretical expectation. Remarkably, the lifetime of the $|20\rangle$ state remains above 1 ms, demonstrating the system's potential as a high-coherence platform supporting Fock states with large photon numbers, a precursor to qudit control.

III. FAULT-TOLERANT STATE PREPARATION WITH SIDEBAND TRANSITIONS

Any two-level ancilla dispersively coupled to a linear system provides the nonlinearity needed for universal control. One widely used approach is the Selective Number-dependent Arbitrary Phase (SNAP) gate combined with unconditional displacement, which can implement arbitrary unitary operations [1, 34]. However, the standard SNAP gate duration should be sufficiently longer than $2\pi/|\chi_e|$, making it inefficient when χ_e is small. In contrast, both the Echoed Conditional Displacement (ECD) gate [35–37] and the sideband control [28, 38, 39], which also enable high-fidelity universal control, with a gate time controlled by microwave drive strength much shorter than the SNAP gate duration limit $2\pi/|\chi_e|$.

In this experiment, we utilize the sideband scheme [28, 38, 40] for controlling the cavities and further develop ancilla-error resilient state preparation schemes. The basic principle of preparing a large Fock state in a single mode is illustrated in Fig. 2(a). The transmon-resonator system is initially in the $|g, 0\rangle$. The transmon is unconditionally excited to the $|f\rangle$ level applying broadband π_{ge} and π_{ef} pulses. Then a sideband $\pi_{\text{sb}}^{(0)}$ pulse at the $|f, 0\rangle \leftrightarrow |g, 1\rangle$ transition is applied to prepare the state $|g1\rangle$. By repeatedly applying a sequence of π_{ge}, π_{ef}, and $\pi_{\text{sb}}^{(n)}$ sideband pulses at $|f, n\rangle \leftrightarrow |g, n+1\rangle$, it is possible to prepare Fock states up to a large photon number. The sideband pulses need not be frequency selective for the purpose of Fock state preparation as well as for certain other superposition states when a recently developed shelving technique [28] is utilized.

In order to estimate the fidelity $\mathcal{F}_n$ of a Fock state with photon number n, one can avoid full tomography as $\mathcal{F}_n$ is equal to the population of the target photon number. We measure the cavity photon population using photon-number-resolved spectroscopy (PNRS), where the probabilities are normalized using the transmon's readout ($|g\rangle$ and $|e\rangle$) values. The population distribution for the Fock 20 is shown in the first panel of Fig. 2(c), with fidelity $\mathcal{F}_{20} = 50.0\%$ limited by the leakage to the lower Fock levels, as a result of decoherence and control errors occurring during the SB protocol.

In climbing the Fock ladder to reach the target photon state, decoherence in both the transmon and cavity can introduce errors during state preparation. Because the cavity coherence time significantly exceeds that of the transmon, and since transmon π pulses in our system are approximately twenty times faster than sideband operations, the fidelity is primarily limited by transmon errors occurring during sideband pulses. Specifically, a transmon decay event from the initial state $|f, n\rangle$ results in the error state $|e, n\rangle$, preventing the sideband transition to $|g, n+1\rangle$; similarly, transmon dephasing disrupts the coherent transition $|f, n\rangle$ to $|g, n+1\rangle$, leaving residual population in $|f, n\rangle$. Although the probability of such events within a single sideband operation is low, the multiple repetitions required to prepare high-photon-number Fock states can cumulatively lead to significant infidelity. To mitigate this cumulative infidelity caused by the ancilla, we have developed a "sideband feedforward protocol" (SFP), illustrated in Fig. 2(b). Akin to other techniques exploiting multi-level transmon readout for fault-tolerant cavity operations [41–45], the SFP leverages error syndrome detection via high-fidelity single-shot measurements of the transmon populations in the $|g\rangle$, $|e\rangle$, and $|f\rangle$ states after each sideband operation. This information is then fed forward to determine the subsequent corrective pulse. A measurement outcome of $|f\rangle$ heralds a dephasing event, which we correct by repeating the same sideband pulse. An outcome of $|e\rangle$ indicates a transmon decay event; in this case, we first apply a π_{ef} pulse and then repeat the sideband pulse to restore the intended state. Finally, an outcome of $|g\rangle$ indicates the ideal scenario where no error has occurred, and thus requires no further correction.

The success of this approach strongly depends on achieving a high-fidelity three-state readout of the transmon. In our system, we achieve over 98% three-state readout fidelity (see Appendix D for details) using a 1.7 μs long readout pulse. By incorporating this SFP protocol, we significantly reduce the residual population in the lower Fock states. As an example, Fig. 2(c) middle panel shows the improvement in population to 82.6% for Fock 20.

Furthermore, we observe that the remaining off-target population after climbing the ladder to Fock N using SFP is mostly found in the $|N-1\rangle$, making it possible to apply a parity filter (PF) and post-select out the $|N-1\rangle$ population for an additional improvement. Specifically, we apply a $\pi_{ge}/2$ pulse at the frequency $\omega_0 + N\chi$, wait for $\pi/|\chi_e|$, then apply a negative $\pi_{ge}/2$ pulse, and finally perform a transmon readout. During the wait time of $\pi/|\chi_e|$, the transmon acquires a phase shift dependent on whether the total photon number in the cavity is even or odd. The final negative $\pi_{ge}/2$ pulse then maps correct parity states to $|g\rangle$ and incorrect parity states to $|e\rangle$. We then discard measurement outcomes where the transmon is found in $|e\rangle$, indicating a parity error. By combining the PF with SFP, we further suppress the off-target population, resulting in a higher preparation fidelity (Fig. 2(c) right panel).

We perform an open-system simulation for the Fock state preparation protocol, with detailed information in Appendix E. The simulation shows that SFP effectively corrects the transmon decoherence errors, which are the main source of infidelities in the SB case. While the SFP infidelity is noticeably improved by correcting the transmon decoherence errors, the remaining infidelity arises primarily from transmon readout errors and qudit relaxation errors caused by the additional readout operations.

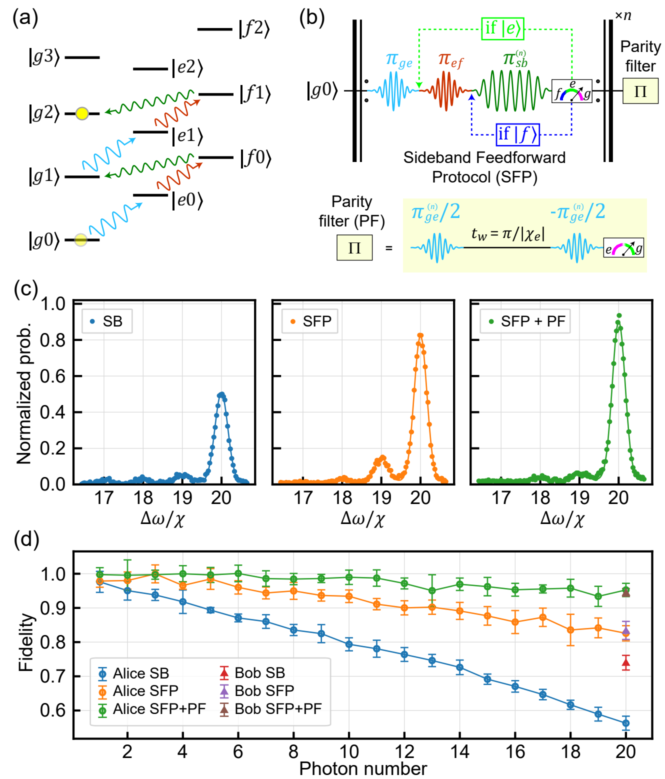

FIG. 2. **Fock state preparation and characterization.** **(a)** Sideband scheme demonstrating the transfer of population starting from $|g0\rangle$ to $|gn\rangle$. Addition of one photon in the bosonic ladder involves application of unconditional π_{ge} (light blue arrows) and π_{ef} (red arrows) pulses on the transmon followed by a π pulse (π_{sb}) at the sideband transition $|f, n\rangle \leftrightarrow |g, n+1\rangle$ (dashed green arrows). **(b)** Pulse protocol for correcting ancilla errors and cavity single-photon loss. After each π_{sb} pulse, the transmon is measured, followed by application of conditional pulses to correct transmon errors, termed as 'sideband feedforward protocol' (SFP). At the end of the sequence, a parity filter (PF) is applied to post-select results with the expected parity. The PF is implemented by applying two opposite $\pi_{ge}/2$ pulses conditioned on n photons with a gap of $\pi/|\chi_e|$ so that the correct state is always mapped to $|g\rangle$. **(c)** Photon-number-resolved spectroscopy (PNRS) of the $|20\rangle$ state, prepared in the Alice mode, using sideband only (left), SFP (middle), and both SFP and PF (right). SFR significantly improves the height of the target peak, with remaining infidelity primarily caused by leakage to the off-target state $|19\rangle$. This error is further suppressed by implementing PF and post-selecting on the correct state. **(d)** Fidelities of different Fock states in the Alice (round markers) and Bob (triangular markers) modes prepared using the three methods. The error-resilient methods clearly improve the state preparation fidelities.

This change in the source of infidelities explains the out-of-target population predominantly observed in the state $|N-1\rangle$ when using SFP compared to a more even out-of-target distribution in the SB case, as shown in Fig. 2(c), since the effective qudit relaxation rate increases with the photon number while the transmon decoherence er-

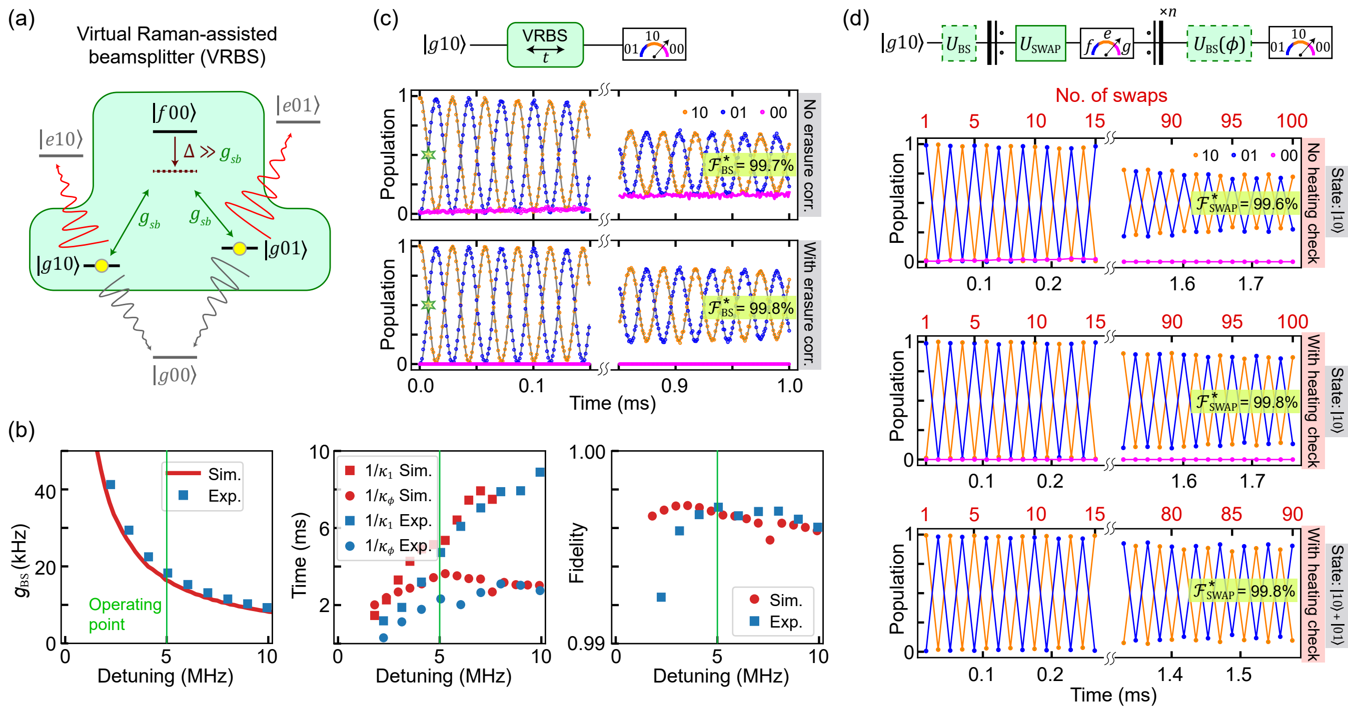

FIG. 3. **Virtual Raman-assisted beamsplitter (VRBS) operation.** **(a)** Level diagram showing microwave drives for realizing the VRBS operation between the two modes and relevant stochastic processes that can lead to errors. The green arrows represent detuned $|f0\rangle \leftrightarrow |g1\rangle$ transition for both modes with rates g_{sb}. The gray lines show single-photon decay channels giving rise to erasure errors. The red lines represent transmon heating events arising due to sideband drives. **(b)** Characterization of VRBS interactions. The three panels show beamsplitter rates, cavity decoherence rates, and gate fidelities as a function of the sideband detuning. Blue and red markers denote experimental data and numerical simulation results, respectively. **(c)** VRBS fringes with the circuit diagram. Top and bottom panels show data before and after discarding cases of erasure error. Fidelity numbers are obtained using Eq. (2). **(d)** Action of swap operations. The transmon is measured after each swap (top panel) and a heating check is performed by not discarding only if it is found in $|g\rangle$. The gate $U_{\rm BS}$ is not applied when the initial state is $|10\rangle$. The extracted swap fidelity improves when heating check is performed (middle panel). The initial state $(|10\rangle + |01\rangle)/\sqrt{2}$ is used to calibrate the phase component of the beamsplitter operation. $U_{\rm BS}$ (bottom panel).

rors are largely insensitive to the photon number. The simulation results indicate that the fidelities of SFP, particularly for high Fock state preparation, can be further enhanced by optimizing transmon readout and reducing qudit relaxation errors.

We plot the state preparation fidelities of Fock states up to twenty photons for Alice and Bob modes, in Fig. 2(d). The traces show clear improvement of the Fock state fidelity obtained with SFP and PF techniques, compared to the vanilla SB protocol. We achieve preparation fidelities of 95.3% and 94.6% for the Fock state $|\psi\rangle_{A/B} = |20\rangle$ in the Alice and Bob modes, respectively. To the best of our knowledge, this represents the highest reported fidelities for such high-photon-number states to date. While we have demonstrated only basis state preparation, sideband control enables arbitrary state synthesis [40, 46] and theoretically supports universal multi-qudit gate operations [39, 47]. Achieving high fidelity and long coherence for large Fock states thus opens new opportunities for qudit-based quantum computation [22, 25, 48–53], quantum sensing [54, 55], and quantum simulation [26, 27, 56–61].

IV. SIDEBAND-MEDIATED VIRTUAL RAMAN INTERACTION FOR CAVITY ENTANGLEMENT

As a demonstration of two-mode control in this cavity system, we extend the sideband approach to implement a two-mode entangling operation, realizing a beamsplitter interaction in the single-photon subspace of the two modes. Such interaction has previously been implemented using either a transmon [62, 63] or a dedicated coupling element to enable three- or four-wave mixing between modes [6, 7]. In contrast to standard four-wave mixing with a fixed frequency transmon, we leverage the transmon's $|f\rangle$ level to mediate the interaction. By simultaneously driving the transmon at a detuning Δ from the $|f0\rangle \leftrightarrow |g1\rangle$ sideband transitions of both Alice and Bob, we activate a virtual-Raman-assisted beamsplitter (VRBS) interaction between the two modes, enabling coherent photon exchange and entanglement (see Fig. 3(a)). Choosing Δ larger than the sideband rates suppresses direct population of the more lossy transmon $|f\rangle$ state during the interaction, albeit at the cost of a reduced conversion rate. Importantly, compared to the standard four-wave mixing protocol, our technique achieves a faster conversion rate for a given drive strength, with an enhancement factor of $|\alpha/\Delta|$, where α is the transmon anharmonicity (see Appendix F).

To estimate the fidelity of the entangling operation, we begin by measuring the evolution of the two modes under the VRBS interaction, with an initial single-photon Fock state in the Alice mode. After an evolution time of t, we turn off the VRBS interaction, and map the two-mode states in the single-photon subspace, specifically $|10\rangle$, $|01\rangle$, and the erasure state $|00\rangle$ (order: Alice $\otimes$ Bob), onto the transmon states $|e\rangle$, $|f\rangle$, and $|g\rangle$, respectively (see Appendix I). This allows us to monitor the evolution of the state populations as a function of time, which can be fitted to the theoretical model described in [7],

$$P_{\mathrm{Bob}} = \frac{1}{2} e^{-\kappa_1 t}(1 + e^{-\kappa_\phi t} \cos(2 g_{\mathrm{BS}} t)), \tag{1}$$

where g_{BS} is the beamsplitter rate, with the corresponding beamsplitter time $\pi/(4g_{\mathrm{BS}})$. The effective decay and dephasing rate of the oscillation, κ_1 and κ_ϕ, together determine the coherence-limited fidelity of the beamsplitter and the swap operations,

$$F^*_{\mathrm{BS}} \approx 1 - \frac{\pi}{4}\frac{\kappa_{\mathrm{BS}}}{g_{\mathrm{BS}}},\ F^*_{\mathrm{SWAP}} \approx 1 - \frac{\pi}{2}\frac{\kappa_{\mathrm{BS}}}{g_{\mathrm{BS}}},\ \kappa_{\mathrm{BS}} = \kappa_1 + \frac{\kappa_\phi}{2} \tag{2}$$

We optimize the fidelity of the cavity entangling operation as a function of the VRBS detuning Δ. For a fixed sideband drive strength g_{SB}, the Raman-assisted beamsplitter rate increases as Δ decreases, as shown by the experimental data in Fig. 3(b, left). However, this enhanced interaction comes at the cost of both increased decay and dephasing. Qualitatively, the beamsplitter rate scales inversely with Δ (see Appendix F), while the sideband-drive-induced Purcell decay follows an approximate Δ^{-2} dependence [29]. This scaling alone would suggest that the total infidelity should decrease with increasing detuning. However, at large detunings, cavity decoherence is no longer limited by sideband-induced decay, but is instead dominated by dephasing due to transmon heating induced by the strong drive tones. This heating arises from undesired parametric processes such as dressed dephasing [64]. A heating event excites the transmon to the $|e\rangle$ state, effectively halting the coherent photon exchange . As a result of the strong transmon-state-dependence of the beamsplitter rate, this introduces statistical dephasing of the VRBS oscillation (see Appendix F). Additionally, transmon heating enhances photon shot noise dephasing of the cavity modes. Since these heating processes are governed by the detuning between the transmon and the drive (on the order of GHz [65]), they are largely insensitive to MHz-scale variations in Δ, leading to the observed saturation of the beamsplitter dephasing time $1/\kappa_\phi$ at large detunings in Fig. 3(b, middle).

The interplay between these mechanisms leads to a maximum in gate fidelity as a function of sideband detuning, as shown in Fig.3 (b, right). We quantitatively capture this trade-off using open-system numerical simulations, from which we extract cavity decoherence times, beamsplitter rates, and the resulting gate fidelities across a range of detunings. The simulated results show good agreement with experimental measurements (see Appendix G for further discussion).

The coherent photon exchange process corresponding to the VRBS interaction at the optimal parameters are shown in Fig.3 (c, top). Fitting this oscillation using Eq. (2) yields a coherence-limited beamsplitter fidelity of 99.7%. This operation can be interpreted as a single-qubit gate on a dual-rail qubit ($\{|10\rangle, |01\rangle\}$) encoded across the single-photon subspace of the two cavity modes [45, 66]. We observe a gradual increase in the population of the $|00\rangle$ state during the interaction as a result of photon loss in the cavity modes, equivalent to the erasure error of a dual-rail qubit. While we do not implement an erasure syndrome measurement that preserves the dual-rail qubit state, we estimate the improvement in fidelity from erasure checks by post-selecting on the absence of erasures at the end of the oscillation. The resulting oscillation, conditioned on no erasure events, exhibits a greatly prolonged decay constant of $1/\kappa_1 = 70.85$ ms, translating to an improved $\mathcal{F}^*_{\mathrm{BS}}$ of 99.8% (Fig. 3(c, bottom)).

In addition to post-selecting on erasure errors, we also perform mid-circuit detection of transmon heating errors, which, as previously discussed, are the dominant source of dephasing in the VRBS operation. These heating errors are detected via a transmon measurement, which—when post-selecting on the transmon being in the ground state—introduces negligible backaction on the cavity states due to the weak hybridization between the transmon and the cavities in our regime. We verify that the cavity Fock state lifetimes are unaffected by repeated transmon measurements in Appendix I. We demonstrate the resulting fidelity improvement using a SWAP operation. To amplify the effect of heating, we apply a sequence of SWAP gates implemented via the same VRBS interaction. As a baseline, Fig. 3(d, top) shows the outcome of this sequence—initialized in $|g10\rangle$—with only a final erasure check. The measured heating rate is found to be approximately 1% per SWAP (See Appendix H). To quantify the benefit of heating error detection, we then perform transmon measurements after each SWAP. The corresponding results, also shown in Fig. 3(d, middle), exhibit a clear improvement in contrast after one hundred SWAPs, corresponding to a two-fold improvement in fidelity (infidelity drop from 0.4% $\rightarrow$ 0.2%). We further verify that this improvement holds for initial states prepared as entangled superpositions of the two modes (i.e., equatorial states on the Bloch sphere in the dual-rail encoding) by applying a U_{BS} following the initialization of a Fock state in one mode (Fig. 3(d, bottom)). We thereby realize a partially error-detected SWAP gate, which can be incorporated mid-circuit to improve the fidelity of shallow-depth algorithms and to support dual-rail surface code implementations [44] using simpler fixed-frequency transmon couplers. This error-detection scheme can also be extended to beamsplitter operations via additional pulse calibration steps that compensate for Stark shift effects [7]. Based on the SWAP gate measurement results, we infer a coherence-limited fidelity of $\mathcal{F}_{\rm BS}^{*} \approx 99.9\%$ for the error-detected beamsplitter gate—comparable to state-of-the-art results, albeit with longer gate durations, but achieved using significantly simpler circuit hardware.

The demonstrated VRBS operation entangles the two cavities within the single-photon subspace. When extended beyond this subspace, the interaction continues to couple states of fixed total photon number and mediates single-photon exchange between the modes. However, the nonlinearity of the transmon introduces photon-number-dependent corrections to the beamsplitter rate, as shown in Appendix F. In particular, the rate is modified because the VRBS detuning for higher-photon-number sectors is altered by their dispersive shift. This nonlinear (non-Gaussian) beamsplitter can serve as a primitive for implementing entangling gates between qudits and for quantum simulations of interacting bosonic systems. For example, in the two-qutrit subspace, five VRBS operations combined with single-qutrit rotations can be used to synthesize the qutrit CSUM gate with 99.1% fidelity (see Appendix J). The potential of this gate operation for universal qudit control will be explored in future work.

V. CONCLUSION

We have demonstrated a superconducting quantum platform that combines ultrahigh coherence with error-resilient control in a two-mode SRF cavity-based circuit QED system. By leveraging sideband interactions and a real-time feedforward protocol, we achieve high-fidelity preparation of Fock states up to $n = 20$, with post-selected fidelities exceeding 95%. We further realize two-mode entangling operations mediated by a virtual Raman transition through the intermediate $|f00\rangle$ state, allowing for coherence-limited beamsplitter fidelities up to 99.9% after post-selection. The current gate speed is limited by the sideband rate, which can be improved through further design and RF wiring optimizations. Extending beyond the single-photon manifold, the ancilla-mediated interaction introduces nonlinear terms in the effective Hamiltonian that may be harnessed for simulating interacting bosonic systems and as primitives for entangling qudit gates—directions we plan to explore in future work. We also aim to investigate the application of feedforward in the context of gate operations.

The elliptical-shaped 2-cell cavity architecture demonstrated in this work can be naturally scaled by increasing the number of cells to realize larger multimode systems. These can be configured into cascaded random access quantum memories [67] with order-of-magnitude improvements in coherence times, where each two-cell module serves as a cache memory. Improved surface treatments [16] can further improve quality factors by an order of magnitude. Additionally, these two-cell devices can function as modular building blocks for a scalable quantum module, leveraging quantum-state router [68] for the exchange of quantum information and the distribution of entanglement. This setup can be further scaled by employing remote interconnection between the scalable modules, and even across different cryogenic systems, facilitating the development of a distributed quantum network with improved coherence and transformative computational power.

ACKNOWLEDGMENTS

The authors acknowledge Edward Pieszchala, Tim Ring, Damon Bice, Michael Foley, Theodore Ill, Mackenzie Ring, and Dominic Baumgart for their support in cavity fabrication, processing, and assembly. Y. L. thanks insightful discussions with J. G. Garmon. The work was supported by the U.S. Department of Energy, Office of Science, National Quantum Information Science Research Centers, Superconducting Quantum Materials and Systems (SQMS) Center under the contract No. DE-AC02-07CH11359. This work made use of the Pritzker Nanofabrication Facility of the Institute for Molecular Engineering at the University of Chicago, which receives support from Soft and Hybrid Nanotechnology Experimental (SHyNE) Resource (NSF ECCS-1542205), a node of the National Science Foundation's National Nanotechnology Coordinated Infrastructure.

Appendix A: System Hamiltonian parameters

In this experiment, there are four bosonic modes involved in the system: two 3D high-Q cavity modes, Alice and Bob, one quasi-planar readout resonator mode, and the weakly nonlinear ancilla transmon mode. The system Hamiltonian can be expressed as

$$\begin{aligned}\hat{\mathcal{H}}/\hbar = {} & \omega_a \hat{a}^\dagger \hat{a} + \omega_b \hat{b}^\dagger \hat{b} + \omega_r \hat{r}^\dagger \hat{r} \\ & + \omega_q |e\rangle\langle e| + (2\omega_q + \alpha)|f\rangle\langle f| \\ & + \chi_e^a\, |e\rangle\langle e| \hat{a}^\dagger \hat{a} + \chi_e^B\, |e\rangle\langle e| \hat{b}^\dagger \hat{b} + \chi_e^R\, |e\rangle\langle e| \hat{r}^\dagger \hat{r}\end{aligned} . \tag{A.1}$$

Values of the Hamiltonian parameters and loss parameters of the system are shown in Table. A1. The inverse-Purcell limit on the cavity mode lifetime is determined by both the relaxation as well as the dephasing channel of the transmon, which can be approximated as [14, 69]

$$T_{1a,b}^{\rm Purcell} \approx \left(\frac{\Delta_{a,b}}{g_{a,b}}\right)^2 \frac{T_{2E}^{ge}}{2}. \tag{A.2}$$

From this, we estimate decay times of $T_{1a}^{\rm Purcell} = 1.17\,{\rm s}$ and $T_{1b}^{\rm Purcell} = 0.34\,{\rm s}$, far exceeding the bare Alice and

Parameter	Description	Value
ω_a	Alice mode frequency	$2\pi \times 5.779$ GHz
T_1^A	Alice mode depolarization time	20.6 ms
T_2^A	Alice mode Ramsey decay time	21.1 ms
$\bar{n}_{\rm th}^a$	Alice mode thermal population	$< 0.1\%$
ω_b	Bob mode frequency	$2\pi \times 6.872$ GHz
T_1^B	Bob mode depolarization time	15.6 ms
T_2^B	Bob mode Ramsey decay time	21.7 ms
$\bar{n}_{\rm th}^b$	Bob mode thermal population	$< 0.1\%$
ω_q	Transmon $\lvert g\rangle \leftrightarrow \lvert e\rangle$ frequency	$2\pi \times 6.402$ GHz
α	Transmon anharmonicity	$-2\pi \times 245$ MHz
T_1^{ge}	Transmon depolarization time	147.4 μs
T_2^{ge}	Transmon dephasing time	47.3 μs
T_{2E}^{ge}	Transmon Hahn-echo coherence time	205.8 μs
$\bar{n}_{\rm th}^q$	Transmon thermal population	0.25%
T_1^f	Transmon $\lvert f\rangle$-state lifetime	80.1 μs
T_2^{gf}	Transmon $(\lvert g\rangle + \lvert f\rangle)$ coherence time	45 μs
g_a	Transmon–Alice vacuum Rabi coupling	$2\pi \times 5.841$ MHz
g_b	Transmon–Bob vacuum Rabi coupling	$2\pi \times 8.114$ MHz
χ_e^a	Transmon–Alice dispersive shift	$-2\pi \times 71$ kHz
χ_e^b	Transmon–Bob dispersive shift	$-2\pi \times 96$ kHz
ω_r	Readout resonator frequency	$2\pi \times 8.379$ GHz
T_1^R	Readout resonator lifetime	266 ns
χ_{qr}	Transmon–readout dispersive shift	$-2\pi \times 411$ kHz
ω_p	Purcell resonator frequency	$2\pi \times 8.529$ GHz

TABLE A1. **Experimentally measured various system parameters.**

Bob lifetime limited by the cavity intrinsic material loss. It's worth noting that this approximation assumes the same dephasing rate measured from the Hahn-echo experiment, for the actual dressed-dephasing-induced cavity decay process, whereas in reality they are sensitive to dephasing noises at very different frequency scales (MHz vs GHz). A more precise understanding of the Inverse-Purcell limit due to the dephasing noise would require probing the dephasing spectral density via spin-locking techniques [70].

We also estimate the cavity dephasing time limit due to the transmon thermal shot noise. In the small thermal population limit, we approximate the thermal-noise-induced cavity dephasing time as [71, 72]

$$T_{\phi a,b}^{\rm th} = \frac{(\chi_e^{a,b})^2 + (T_1^{ge})^{-2}}{\bar{n}_{\rm th}^q (T_1^{ge})^{-1} (\chi_e^{a,b})^2}. \tag{A.3}$$

Plugging in parameters in Table. A1, we obtain $T_\phi^{\rm th} = 59$ ms for both modes, reasonably close to the measured cavity dephasing times.

Appendix B: Cavity fabrication and loss characterization

The cavity is CNC-machined from high residual resistivity ratio (RRR$\sim$ 300) grade high-purity Niobium in three separate parts, which are then electron-beam welded along the equators to eliminate seams at the joints. The cavity undergoes a buffered chemical polishing (BCP) process, removing approximately 120 μm

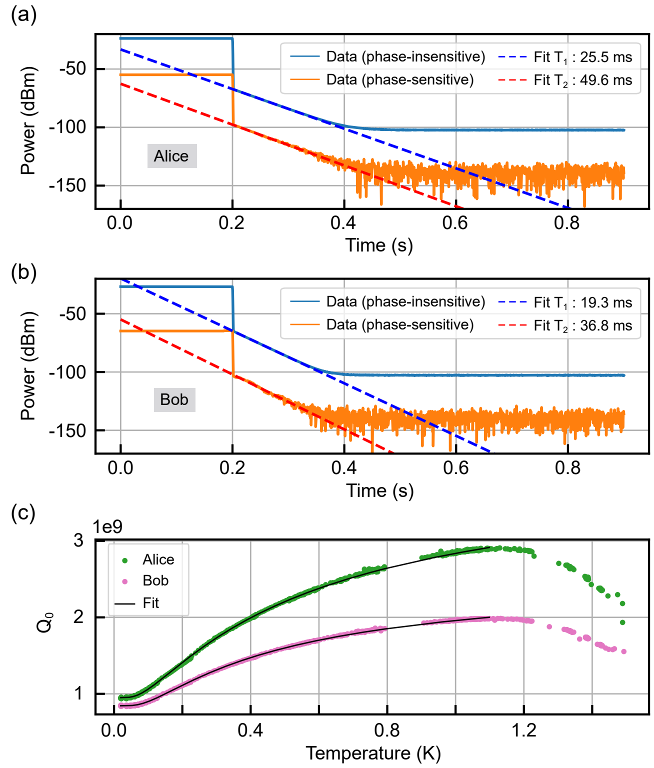

FIG. A1. **Bare cavity characterization. (a)** Ringdown measurements for the Alice mode with showing raw data and linear fits. **(b)** Similar measurements for the Bob mode. **(c)** Internal quality factors as a function of mixing chamber plate's temperature for both modes and fitting to the TLS model.

of material to eliminate mechanical damage and embedded contaminants introduced during manufacturing. Afterward, it is cleaned with a high-pressure water rinse and vacuum-baked for three hours at 800°C to remove hydrogen absorbed into the Niobium during the BCP treatment.

To assess the intrinsic performance of our cavity, we conduct characterization measurements of the bare cavity at 8 mK. We observe (loaded) energy relaxation times of 25.545 ms ± 9 μs for the Alice mode and 19.299 ms ± 4 μs for the Bob mode using ringdown measurements performed with a vector network analyzer. Figure A1(a-b) show power emitted from the cavity modes measured in two distinct ways–phase-insensitive and phase-sensitive. The phase-insensitive traces are obtained by first measuring the power using squared sum of the I/Q values at a given time followed by averaging many such data points. The phase-sensitive traces are obtained by reversing the order, namely, taking the average of individual I and Q values separately and then obtaining square-sum to obtain the power. We extract the pure dephasing times of about 1810 ms and 790 ms of the bare cavity modes using the methodology introduced in [73] by utilizing these measurements.

Additionally, we perform a temperature sweep to investigate the temperature dependence of internal quality factor (Q_0), allowing extraction of the zero-temperature loss tangent(δ_0) associated with two-level systems (TLS), the residual surface resistance(R_{res}) [16], and temperature measurement efficiency (β) using the following function

$$\frac{1}{Q_0(T)} = F\delta_0 \tanh\left(\beta\frac{\hbar\omega}{2k_BT}\right) + \frac{R_{\text{res}}}{G}, \quad \text{(B.1)}$$

where T is the temperature in Kelvin, F is the surface oxide filling factor, and G is the geometry factor calculated from finite-element simulations. At each temperature point, we perform a ring-down measurement to extract the loaded quality factor, Q_L. We then calculate the internal quality factor Q_0, from this Q_L in conjunction with the coupling quality factor Q_{ext} obtained from circle fitting at base temperature. The relevant parameters are shown in Table A2. The measured residual surface resistance is higher than that typically observed in standard SRF cavities[74, 75], suggesting the presence of residual contaminants on the cavity surface. Subsequent studies with different cavities confirmed the likely presence of such contamination in the furnace used for the cavity preparation. Based on this, elimination of these additional losses can be achieved by an extra buffered chemical polishing (BCP) etching to remove the embedded contaminants. Furthermore, we plan to reduce the TLS losses coming from surface oxide via enhanced surface treatment techniques developed previously [16]. The most recent progress of SQMS (manuscript in preparation) includes demonstrating the ability to grow an air-exposure robust oxide with the drastically suppressed TLS density, which should allow a further multifold increase in the cavity quality factor. These combined improvements should allow at least an order of magnitude improvement in the energy relaxation times of both Alice and Bob modes.

f_0 (GHz)	G (Ω)	$R_{\text{res}}(n\Omega)$	$F\delta_0$	F	δ_0
5.779 (Alice)	295	73.4	8.0×10^{-10}	6.7×10^{-9}	0.12
6.872 (Bob)	298	121.9	7.9×10^{-10}	1.5×10^{-8}	0.05

TABLE A2. **Extracted parameters from fitting the TLS model.**

Appendix C: Minimization of transmon induced losses

Our cavity design leverages the established TESLA geometry, commonly employed in particle accelerators, providing inherent advantages such as a small surface oxide filling factor ($< 2\times10^{-8}$) and a large geometry factor ($\approx 270, \Omega$). These characteristics significantly reduce dielectric and surface losses, enhancing cavity coherence. However, coupling the inherently lossy transmon chip to the cavity introduces various loss channels, including dielectric and surface losses.

In this section, we outline two complementary strategies to minimize losses induced by the transmon chip: reducing the transmon-cavity dispersive shift and strategically positioning the transmon frequency near the straddling regime. These approaches enable an optimal balance between achieving a strong dispersive shift and minimizing inverse-Purcell losses. Using finite-element simulations, we calculate the loss channel participation ratios p_{bulk}, p_{MA}, p_{SA}, and p_{MS}. Following the methodology outlined in [76], we estimate the transmon chip's bulk loss rate as $\kappa_{\text{bulk}} = \omega_c p_{\text{bulk}} \tan\delta_{\text{bulk}}$ and surface loss rate as $\kappa_{\text{surf}} = \omega_c \sum_{i=\text{MS,MA,SA}} p_i \tan\delta_i$. We evaluate these loss rates as functions of the dispersive shift and transmon frequency, as summarized in Table A3. Our analysis indicates that, under the current parameter configuration, material losses do not impose significant limitations on the cavity T_1 performance.

$$p_{\text{bulk}} = \frac{\int_{\text{bulk}} \epsilon|\vec{E}|^2 dv}{\int_{\text{all}} \epsilon|\vec{E}|^2 dv} \quad \text{(C.1)}$$

$$p_{\text{MA}} = \frac{t_{\text{surf}} \int_{\text{MA}} \epsilon_0|\vec{E}|^2 d\sigma}{\epsilon_{\text{r,MA}} \int_{\text{all}} \epsilon|\vec{E}|^2 dv} \quad \text{(C.2)}$$

$$p_{\text{SA,MS}} = \frac{t_{\text{surf}} \int_{\text{SA,MS}} \epsilon|\vec{E}|^2 d\sigma}{\int_{\text{all}} \epsilon|\vec{E}|^2 dv} \quad \text{(C.3)}$$

Transmon	**Alice**			**Bob**		
$\omega_{ge}/2\pi$ (MHz)	$\chi_e^a/2\pi$ (kHz)	$\kappa_{\text{bulk}}/2\pi$ (Hz)	$\kappa_{\text{surf}}/2\pi$ (Hz)	$\chi_e^B/2\pi$ (kHz)	$\kappa_{\text{bulk}}/2\pi$ (Hz)	$\kappa_{\text{surf}}/2\pi$ (Hz)
6714	-21	0.017	0.004	-150	0.604	0.178
6434	-58	0.027	0.007	-68	0.101	0.014
6304	-120	0.036	0.009	-43	0.065	0.017

TABLE A3. Transmon chip induced loss rates for cavity modes.

Appendix D: Transmon readout fidelity

The frequency, amplitude and length of the readout pulse is optimized to maximize the 3-state discrimination probabilities for the transmon. A Josephson parametric amplifier (JPA) with about 17.7 dB gain is used to amplify the readout signal at the base temperature. The IQ blobs and demarcation lines for the $|g\rangle, |e\rangle$ and $|f\rangle$ levels are pictured in Fig. A2(a). This mapping is used for making decisions in the SFP protocol for correcting ancilla errors during Fock state preparations. The corresponding confusion matrix is shown in Fig. A2(b) resulting in an overall readout fidelity of 0.9876.

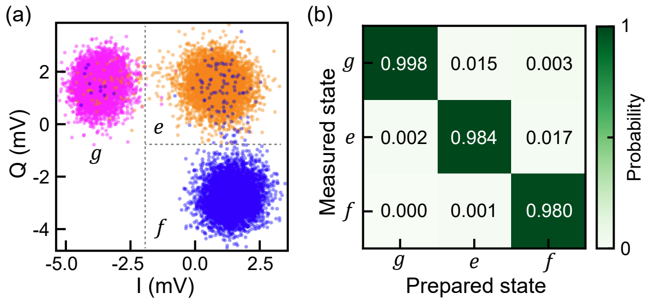

FIG. A2. **Three-level readout of the transmon. (a)** IQ blobs and demarcation lines for $|g\rangle, |e\rangle$ and $|f\rangle$ states. **(b)** Resulting confusion (assignment) matrix.

Appendix E: Fidelity estimations for SFP

This appendix presents an open-system simulation of the fault-tolerant state preparation protocol discussed in Sect. III conducted by classical computers. The simulation results indicate that the sideband feedforward protocol (SFP) nearly completely corrects decoherence errors in the ancilla transmon qubit. However, this comes at the cost of introducing additional errors due to transmon decoherence and measurement errors. This trade-off directly results in the dominant peak of the $(N-1)$ out-of-target population, as shown in Fig. 2 and confirmed by simulation. In the following subsections, we will explain the noise model used in the simulation and discuss the insights the simulation results provide.

1. Noise model

In the following, we will discuss a noise model for the transmon readout error and the decoherence effects of both the qudit and the ancilla transmon qubit based on the calibration data presented in Table A1.

All unitary operations performed for the state preparation are rotations between two levels, $\hat{R}_{j,k}(\theta)$, where j and k are level indices of the qudit-transmon system and θ is the rotation angle. For example, the sideband transition is given as $\hat{R}_{ne,(n+1)g}(\pi/2)$. Here, without loss of generality, we construct the rotation unitaries analogous to the qubit rotation along the y-axis as

$$\begin{aligned}\hat{R}_{j,k}(\theta) =& (|j\rangle\langle j| + |k\rangle\langle k|)\cos\frac{\theta}{2} + (|k\rangle\langle j| - |j\rangle\langle k|)\sin\frac{\theta}{2} \\ &+ \sum_{\ell\neq j,k} |\ell\rangle\langle\ell|. \end{aligned} \tag{E.1}$$

Different choices of rotation unitary construction correspond to different pulse realizations of transition operations between two levels, which result in different phases for the two levels. However, this difference does not affect the simulated fidelity of our Fock state preparation protocol. Hence, we pick a specific construction for all rotations. Without noise, the rotation operations modify the system state $|\psi\rangle$ such that

$$|\psi\rangle \rightarrow \hat{R}_{j,k}(\theta)|\psi\rangle. \tag{E.2}$$

We use the Lindblad master equation [77] to simulate the Fock state preparation protocol with noise. The Lindblad master equation, which governs the time evolution of the system density matrix ρ, can be written as

$$\frac{\mathrm{d}\rho}{\mathrm{d}t} = -i[\hat{H}(t), \rho] + \sum_{\alpha} \hat{\mathcal{D}}[\hat{A}_\alpha]\rho, \tag{E.3}$$

Here, $\hat{\mathcal{D}}[\hat{A}_\alpha]$ is the Lindblad superoperator given by $\hat{\mathcal{D}}[\hat{A}]\rho = \hat{A}\rho\hat{A}^\dagger - \frac{1}{2}\hat{A}^\dagger\hat{A}\rho - \frac{1}{2}\rho\hat{A}^\dagger\hat{A}$, each jump operator $\hat{A}_\alpha$ is associated with a decoherence channel to be discussed in the next paragraph, $\hat{H}(t)$ is the system and control Hamiltonian generating the rotation operation such that

$$\hat{R}_{j,k}(\theta) = \mathcal{T}\int_0^T \mathrm{d}t e^{-i\hat{H}(t)t}, \tag{E.4}$$

where T is the gate time. The noisy rotation operations $\hat{\mathcal{N}}_{j,k}(\theta)$ evolves the system density matrix such that

$$\rho \rightarrow \hat{\mathcal{N}}_{j,k}(\theta)\rho. \tag{E.5}$$

By assuming that the rotation angle is directly proportional to the gate time, $\hat{\mathcal{N}}_{j,k}(\theta)$ can be approximated with a second-order symmetric trotterization such that

$$\hat{\mathcal{N}}_{j,k}(\theta) \approx \left(\hat{\mathcal{R}}_{j,k}(\tfrac{\theta}{2m})\left[1 + \tfrac{T}{m}\sum_{\alpha}\hat{\mathcal{D}}(\hat{A}_\alpha)\right]\hat{\mathcal{R}}_{j,k}(\tfrac{\theta}{2m})\right)^m, \tag{E.6}$$

where m is the trotterization step and $\hat{\mathcal{R}}_{j,k}(\theta)$ is the superoperator corresponding to the unitary rotation operation such that

$$\hat{\mathcal{R}}_{j,k}(\theta)\rho = \hat{R}_{j,k}(\theta)\rho\hat{R}^\dagger_{j,k}(\theta). \tag{E.7}$$

We determined numerically that a value of $m = 4$ is adequate for our simulation.

The transmon depolarization and the thermal heating for the ancilla transmon qubit with three levels are modeled by the jump operators

$$\hat{A}_{T_1^q} = \sqrt{\gamma_{T_1^{ge}}(1 + \bar{n}^q_{\mathrm{th}})}(\sqrt{2}|e\rangle\langle f| + |g\rangle\langle e|), \tag{E.8}$$

$$\hat{A}_{T_1^q,\mathrm{th}} = \sqrt{\gamma_{T_1^{ge}}\bar{n}^q_{\mathrm{th}}}(\sqrt{2}|f\rangle\langle e| + |e\rangle\langle g|), \tag{E.9}$$

(E.10)

where $\gamma_{T_1^{ge}} = 1/T_1^{ge}$ is the transmon decay rate, and $\bar{n}^q_{\mathrm{th}}$ is the average thermal population. For the transmon pure dephasing, we use the model for a three-level system discussed in reference [78] that two jump operators describe the pure phasing,

$$\hat{A}_{T_\varphi^q,f} = \sqrt{2\gamma_{T_\varphi^{ge}}}|f\rangle\langle f|, \tag{E.11}$$

$$\hat{A}_{T_\varphi^q,e} = \sqrt{\gamma_{T_\varphi^{ge}}}|e\rangle\langle e|, \tag{E.12}$$

where $\gamma_{T_\varphi} = 1/T_2^{ge} - 1/(2T_1^{ge})$ is the transmon pure dephasing rate. The factor $\sqrt{2}$ associated with the f state comes as an approximation from the ratio between the noise sensitivity of the $f-g$ energy difference and that of the $e-g$ energy difference, and more detailed discussions of the estimation of the dephasing time of the qubit can be found in references [79, 80]. For the Alice-mode qudit, we write the jump operators for depolarization and pure dephasing as

$$\hat{A}_{T_1^A} = \sqrt{\gamma_{T_1^A}}\hat{a}, \tag{E.13}$$

$$\hat{A}_{T_\varphi^A} = \sqrt{\gamma_{T_\varphi^A}}\hat{a}^\dagger\hat{a}, \tag{E.14}$$

where $\gamma_{T_1^A} = 1/T_1^A$ is the Alice-mode decay rate and $\gamma_{T_\varphi^A} = 1/T_2^A - 1/(2T_1^A)$ is the Alice-mode pure dephasing rate. The jump operators associated with the Bob-mode qudit can be written similarly.

We also take into account the transmon readout fidelity, which introduces error to the SFP, as the correction is conditional on the ancilla transmon qubit readout. While the confusion matrix shown in Fig. A2 is sufficient for readout mitigation, it does not distinguish between the transmon-relaxation-induced readout error, which SFP can partially correct, and the classification error, which SFP cannot correct. To more accurately estimate the readout-related error, we model the readout fidelity using a transmon relaxation probability, denoted as p_{readout}, along with symmetric classification error probabilities. We optimize both the transmon relaxation probability and the classification error probabilities to best match the experimentally measured confusion matrix. This yields the following results: $p_{\text{readout}}(e \to g) = 0.0055$, $p_{\text{readout}}(f \to e) = 0.0110$, and the classification error rate array

$$\begin{bmatrix} 0.9976 & 0.0024 & 0.0000 \\ 0.0024 & 0.9966 & 0.0010 \\ 0.0000 & 0.0010 & 0.9990 \end{bmatrix}. \tag{E.15}$$

Note that the experimentally measured confusion matrix used for optimization is slightly different from the one shown in Fig. A2 due to parameter drift. During the transmon readout, we also take into account the qudit's idling by including the corresponding depolarization and dephasing effects over the readout time of approximately 1700 ns in the simulation.

2. Simulation results

The simulated population distributions shown in Fig. A3(a) are consistent with the experimental results shown in Fig. 2(c). In particular, vanilla SB demonstrates a nearly even distribution for the off-target states, while SPF exhibits a distinct peak at $|N-1\rangle$. This can be explained as follows: although the SFP effectively corrects most transmon errors, the lengthy readout time for each transmon (approximately 1700 ns) involved in the correction process makes uncorrected qudit decoherence errors more prominent. In contrast to the photon-number insensitive transmon errors, which result in nearly uniform off-target populations, the effective error rates for qudits tend to increase with the photon number. Consequently, the off-target distribution is skewed towards N. In the simulation, the $|N-1\rangle$ peak is completely suppressed by PF, while it remains visible in the experimental data. This discrepancy arises because we do not account for the parity filtering efficiency in the simulation.

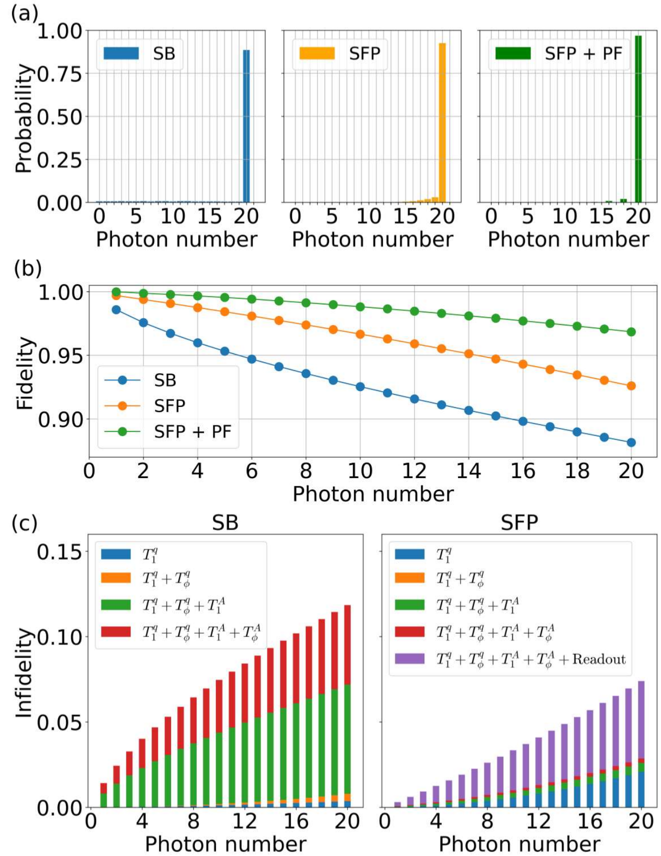

FIG. A3. **Fock state preparation simulation for the Alice-mode qudit. (a)** Simulated qudit population to prepare $|n=20\rangle$ Fock state. **(b)** Simulated fidelities improved by SPF and further improved by PF. **(c)** Ceiling analysis of the error sources.

The predicted fidelities shown in Fig. A3(b) are higher than the experimental results presented in Fig. 2(d). This discrepancy is expected because our noise model is incomplete. In particular, control errors are not calibrated, and thus are not included in the noise model for simulation. The absence of control errors in the noise model is likely the reason why the trend of the predicted SB's fidelities decreases at a slower rate than linear with increasing photon numbers. In contrast, the experimental fidelities show a faster-than-linear decrease as the photon number increases. In the simulation, the decoherence errors are approximately proportional to the sideband transition time, which decreases as $1/|\chi_e| \sim 1/\sqrt{N}$. However, as we move to higher photon numbers, we expect the control errors to become more pronounced as a result of the increasingly crowded energy levels. Therefore, it is likely that the control errors account for the faster-than-linear decrease in the experimental fidelities.

As we discussed earlier, SFP effectively corrects nearly all transmon decoherence errors, albeit at the cost of increasing qudit decoherence errors. This understanding is supported by the ceiling analysis illustrated in Figure A3(c). In our ceiling analysis, we toggle specific noise channels on and off. For instance, the red line demonstrates the difference in fidelities when transmon pure dephasing is on compared to when it is off. This approach allows us to estimate the contributions of transmon pure dephasing and other noise sources to the overall infidelities. Comparing the SFP ceiling analysis on the right with the SB one on the left, the analysis clearly shows the effectiveness of SFP in correcting the transmon decoherence errors (red and green). Meanwhile, readout error (purple) and qudit depolarization (blue) become the limiting factors in the Fock state preparation protocol with SFP. This indicates that achieving higher fidelities and preparing higher Fock states will require further improvements in the ancilla transmon readout fidelity and the qudit T_1, in addition to the control errors mentioned above.

Appendix F: Raman-assisted beamsplitter interaction

Here we derive the Alice-Bob beamsplitter interaction in the virtual Raman protocol. The Hamiltonian of the driven system is

$$\begin{aligned}\hat{\mathcal{H}}/\hbar &= \omega_a \hat{a}^\dagger \hat{a} + \omega_b \hat{b}^\dagger \hat{b} + \omega_{q0} \hat{q}^\dagger \hat{q} \\ &- E_J \cos_{\mathrm{nl}} \left[\theta_q \left(\hat{q} + \frac{g_a}{\Delta_a} \hat{a} + \frac{g_b}{\Delta_b} \hat{b} \right) + \mathrm{h.c.} \right] \\ &+ \sum_{k=1,2} \epsilon_k \cos(\omega_k t) \left(\hat{q} + \hat{q}^\dagger \right), \end{aligned} \tag{F.1}$$

where $g_{a(b)}$ and $\Delta_{a(b)}$ stand for the coupling strength and detuning between Alice(Bob) and the transmon, and $\cos_{\mathrm{nl}}$ stands for 4-th and higher-order components of the cosine function. $\epsilon_{1(2)}$ and $\omega_{1(2)}$ are the amplitudes and frequencies of the two sideband drives acting on the transmon. Going into the displaced frame with respect to the sideband drives,

$$\begin{aligned}\hat{\mathcal{H}}_{\mathrm{disp}}/\hbar &= \omega_a \hat{a}^\dagger \hat{a} + \omega_b \hat{b}^\dagger \hat{b} + \omega_{q0} \hat{q}^\dagger \hat{q} \\ &- E_J \cos_{\mathrm{nl}} \left[\theta_q \left(\hat{q} + \sum_{k=1,2} \xi_k e^{-i\omega_k t} + \frac{g_a}{\Delta_a} \hat{a} + \frac{g_b}{\Delta_b} \hat{b} \right) + \mathrm{h.c.} \right], \end{aligned} \tag{F.2}$$

where $\xi_{1,2}$ represents the drive-induced displacements. We further set the drive frequencies to be $\omega_{1(2)} = 2\omega_{q0} + \alpha - \omega_{a(b)} - \Delta$ to match the VRBS resonance condition, where α is the transmon anharmonicity, and Δ is the virtual level detuning from $|f00\rangle$. From going to the rotating frame and collecting the relevant slow-oscillating terms in $\cos_{\mathrm{nl}}$ expansion, we may approximate the virtual Raman (VR) Hamiltonian as

$$\begin{aligned}\hat{\mathcal{H}}_{\mathrm{VR}}/\hbar \approx& \frac{\alpha}{2} \hat{q}^\dagger \hat{q}^\dagger \hat{q} \hat{q} + \chi_a \hat{q}^\dagger \hat{q} \hat{a}^\dagger \hat{a} + \chi_b \hat{q}^\dagger \hat{q} \hat{b}^\dagger \hat{b} \\ &- \frac{E_J \theta_q^4}{2} \hat{q}^{\dagger 2} \left(\frac{\xi_1 g_a}{\Delta_a} \hat{a} + \frac{\xi_2 g_b}{\Delta_b} \hat{b} \right) e^{-i\Delta t} \\ &- \frac{E_J \theta_q^4 \xi_1 \xi_2^* g_a g_b}{4\Delta_a \Delta_b} \hat{a} \hat{b}^\dagger + \mathrm{h.c.}, \end{aligned} \tag{F.3}$$

where the second line represents the direct Alice-Bob beamsplitter interaction mediated by the 4th-order nonlinearity. By doing second order perturbation theory to eliminate the virtual states, we the total effective beamsplitter interaction between Alice and Bob in the $\{|10\rangle, |01\rangle\}$ subspace to be

$$\hat{\mathcal{H}}_{\mathrm{VR}}^{\mathrm{BS}}/\hbar \approx \left(\frac{E_J^2 \theta_q^8 \xi_1 \xi_2^* g_a g_b}{2\Delta_a \Delta_b \Delta} - \frac{E_J \theta_q^4 \xi_1 \xi_2^* g_a g_b}{4\Delta_a \Delta_b} \right) \hat{a} \hat{b}^\dagger + \mathrm{h.c.} \tag{F.4}$$

$$\approx \left(\frac{2\alpha}{\Delta} + \frac{1}{2} \right) \frac{\alpha \xi_1 \xi_2^* g_a g_b}{\Delta_a \Delta_b} \hat{a} \hat{b}^\dagger + \mathrm{h.c.}. \tag{F.5}$$

This clearly shows that, comparing to the direct four-wave-mixing beamsplitter rate (represented by the 1/2 term), the VR scheme possesses a significant enhancement factor of α/Δ, making it over an order of magnitude faster than the former scheme in our experiment.

While this captures the essential interaction underlying the VR scheme, accurately modeling the system dynamics requires incorporating drive-induced or nonlinear interactions, which we derive below. We apply a Schrieffer-Wolff transformation [81] with a generator of $\hat{\mathcal{S}} = \sum_{n=0,m=0} (\hat{\mathcal{S}}_{n,m}^{(a)} + \hat{\mathcal{S}}_{n,m}^{(b)})$, where

$$\begin{aligned}\hat{\mathcal{S}}_{n,m}^{(a,b)} =& -\frac{E_J\theta_q^4 g_{a,b}\sqrt{2(n+1)}}{2\Delta_{a,b}[\Delta+2(n+m)\chi]}|f,n,m\rangle\langle g,n+1,m|e^{-i[\Delta+2(n+m)\chi]t} \\ &+\frac{E_J\theta_q^4 g_{a,b}\sqrt{2(n+1)}}{2\Delta_{a,b}[\Delta+2(n+m)\chi]}|g,n+1,m\rangle\langle f,n,m|e^{i[\Delta+2(n+m)\chi]t} \\ &-\frac{E_J\theta_q^4 g_{a,b}\sqrt{2(n+1)}}{2\Delta_{a,b}[\Delta+\alpha+(2n+2m-1)\chi]}|h,n,m\rangle\langle e,n+1,m|e^{-i[\Delta+\alpha+(2n+2m-1)\chi]t} \\ &+\frac{E_J\theta_q^4 g_{a,b}\sqrt{2(n+1)}}{2\Delta_{a,b}[\Delta+\alpha+(2n+2m-1)\chi]}|e,n+1,m\rangle\langle h,n,m|e^{i[\Delta+\alpha+(2n+2m-1)\chi]t}.\end{aligned} \tag{F.6}$$

The term in Eq. (F.3) transforms as

$$\begin{aligned}&\sum_{n,m}\frac{E_J^2\theta_q^8\xi_1\xi_2^* g_a g_b}{2\Delta_a\Delta_b}\left(\frac{|g\rangle\langle g|}{\Delta+(2n+2m)\chi}-\frac{|f\rangle\langle f|}{\Delta+(2n+2m+2)\chi}+\frac{|e\rangle\langle e|}{\Delta+\alpha+(2n+2m-1)\chi}-\frac{|h\rangle\langle h|}{\Delta+\alpha+(2n+2m+1)\chi}\right) \\ &\otimes\sqrt{(n+1)(m+1)}(|n,m+1\rangle\langle n+1,m|+|n+1,m\rangle\langle n,m+1|).\end{aligned} \tag{F.7}$$

From the equation above, we note that the beasmplitter rate is highly dependent on the transmon state, with detunings in the energy denominator differing by the anharmonicity.

When the transmon is in the ground state, the expression above can be approximated by the following operator equation in the regime where $\chi \ll \Delta$:

$$\frac{E_J^2\theta_q^8\xi_1\xi_2^* g_a g_b}{2\Delta\Delta_a\Delta_b}|g\rangle\langle g|\otimes(\hat{a}\hat{b}^\dagger+\hat{a}^\dagger\hat{b})\left[1-\frac{2\chi}{\Delta}(\hat{n}_a+\hat{n}_b-1)\right]. \tag{F.8}$$

The beamsplitter rate is modified because the drive detuning to the virtual states (VRBS detuning) for higher-photon-number sectors are altered by their dispersive shifts. This nonlinear correction to the beamsplitter gate has applications in universal qudit control, as discussed in Appendix J.

Appendix G: Numerical simulation of VR entanglement

Here, we provide details on the numerical simulations of the Raman-assisted beamsplitter dynamics. The Hamiltonian in the bare basis is

$$\begin{aligned}\hat{H}/\hbar =& \omega_a\hat{a}^\dagger\hat{a}+\omega_b\hat{b}^\dagger\hat{b}+\omega_q\hat{q}^\dagger\hat{q}-E_J\cos_{\rm nl}\left[\theta_q\left(\hat{q}^\dagger+\hat{q}\right)\right] \\ &+g_a(\hat{a}^\dagger+\hat{a})(\hat{q}^\dagger+\hat{q})+g_b(\hat{b}^\dagger+\hat{b})(\hat{q}^\dagger+\hat{q}) \\ &+\sum_{k=1,2}\epsilon_k\cos(\omega_k t)\left(\hat{q}+\hat{q}^\dagger\right).\end{aligned} \tag{G.1}$$

The circuit parameters are chosen such that the static energy spectrum of the Hamiltonian reproduces the experimental values listed in Table. A1.

Next, we calibrate the sideband drives for Alice and Bob individually. For a fixed sideband amplitude (e.g., ϵ_1), we sweep the corresponding drive frequency ω_1 to extract the resonant $|f0\rangle$–$|g1\rangle$ sideband oscillation period between Alice and the ancilla. This procedure is repeated until the simulated resonant oscillation period matches the experimentally observed value, thereby determining both the sideband drive amplitude ϵ_1 and frequency ω_1. As an example, Fig. A4(a) shows the simulated sideband dynamics for Alice and ancilla. The red lines indicate the resonant conditions, and the corresponding frequency line cuts are shown in Fig. A4(b).

With these calibrated parameters, we simulate the system evolution under simultaneous sideband drives, with identical detunings from their respective resonances. Figure A4(c) displays the resulting population exchange between Alice and Bob, conditioned on the ancilla being in the ground state. For illustration, Fig. A4(d) shows representative line cuts at several detunings. At large detunings, the population exhibits sinusoidal oscillations. As the detuning decreases, the oscillation frequency increases and develops a high-frequency modulation. This modulation is attributed to off-resonant transmon excitation. For instance, the transmon population at a detuning of −1.3 MHz, shown as a dashed line, aligns with the modulation observed in the corresponding beamsplitter dynamics. Figure 3(b) plots the extracted beamsplitter rates as a function of detuning (red line), showing excellent agreement with experimental data (blue dots).

While the above simulations capture the coherent dynamics, we also perform open-system simulations to study decoherence and its effect on gate fidelity. These are based on solving the Lindblad master equation with

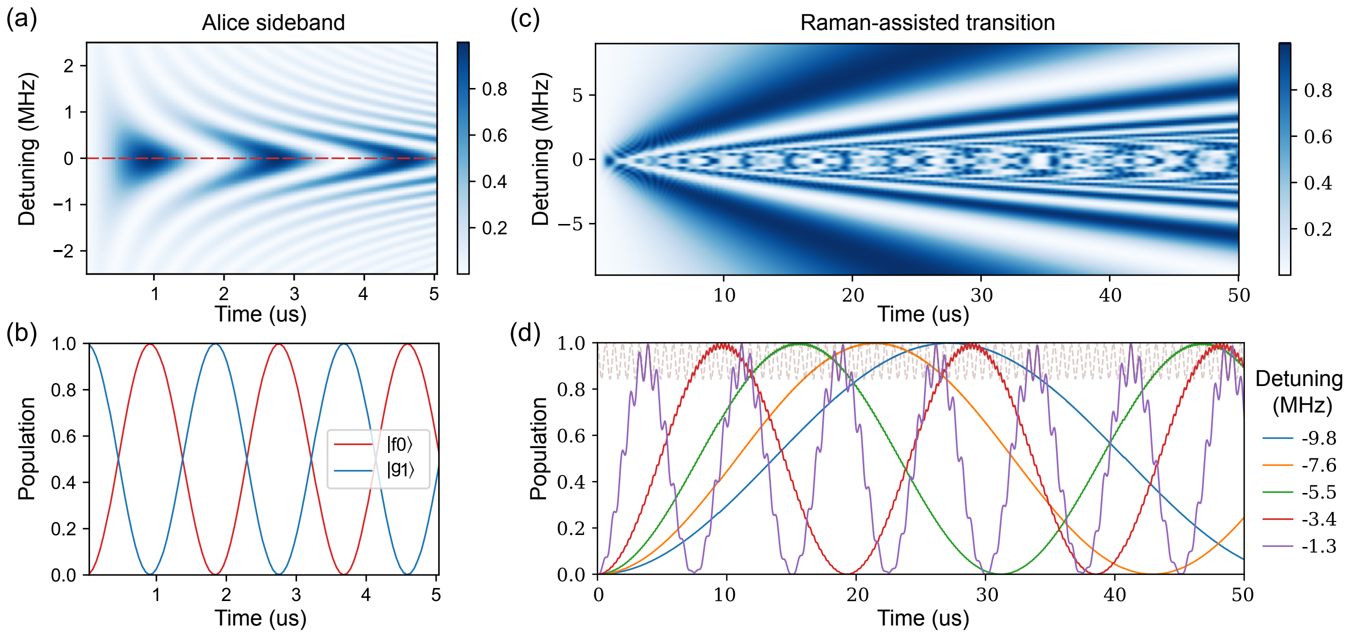

FIG. A4. **Numerical simulations of Raman-assisted beamsplitter interactions. (a)** Simulated $|f0\rangle \leftrightarrow |g1\rangle$ sideband dynamics between Alice and the ancilla as a function of drive detuning. **(b)** Line cuts taken along the resonant sideband condition indicated by the red dashed line in (a). **(c)** Simulated Raman-assisted population exchange between Alice and Bob, mediated by the ancilla and driven by dual sideband tones. **(d)** Line cuts of the cavity population dynamics at representative detunings. The dashed curve shows the transmon population at a detuning of -1.3 MHz, which aligns with the modulation observed in the corresponding cavity population.

the following bare-basis Lindbladian:

$$\begin{aligned}\hat{\mathcal{L}}[\rho]/\hbar =& -i[\hat{H},\rho] + (T_1^{ge})^{-1}\hat{\mathcal{D}}[\hat{q}]\rho \\ &+ \bar{n}_{\text{th}}^{\text{q}}(T_1^{ge})^{-1}\hat{\mathcal{D}}[\hat{q}^\dagger]\rho + 2(T_\phi^{ge})^{-1}\hat{\mathcal{D}}[\hat{q}^\dagger\hat{q}]\rho \\ &+ (T_1^{\text{A}})^{-1}\hat{\mathcal{D}}[\hat{a}]\rho + (T_1^{\text{B}})^{-1}\hat{\mathcal{D}}[\hat{b}]\rho.\end{aligned} \tag{G.2}$$

The decoherence parameters are set to: $T_1^{ge} = 168\mu$s, $\bar{n}_{\text{th}}^{\text{q}} = 4\%$, $T_2^{ge} = 700\ \mu$s, $T_1^{\text{A}} = 26$ ms, and $T_1^{\text{B}} = 20$ ms, which are fitted to reproduce experimental results from individual sideband for Alice and Bob. It is important to note that the ancilla thermal population and dephasing time used here differ from the values reported in Table A1. This discrepancy arises because the Lindblad formalism assumes a white noise spectral density for ancilla pure dephasing, whereas real physical noise spectra are typically $1/f$ in the low-frequency regime. In driven systems, relevant decoherence rates are evaluated at different frequencies: for instance, dressed dephasing—which sets the ancilla's thermal population and induces photon shot noise—samples the noise spectrum at the ancilla–drive detuning (∼GHz); and sideband-dressed ancilla dephasing contributes to cavity decay at frequencies near the sideband detuning (∼MHz). To mimic these effects within the white-noise Lindblad model, we manually adjust the ancilla thermal population to reflect the photon shot noise and reduce its pure dephasing rate to reflect the suppressed noise at larger frequencies.

To extract the cavity T_1 and T_ϕ from numerical simulations, we trace the ancilla to obtain the populations of Alice and Bob as a function of time. Then, we fit the decay oscillation with Eq. (1). Figure 3(b) shows the extracted cavity T_1 and T_ϕ as functions of sideband detuning, which align well with the experiment. Both decay and dephasing times decrease as the system approaches the sideband resonance, consistent with enhanced decoherence due to the sideband drive. Notably, T_ϕ saturates at large detunings, a behavior attributed to photon shot noise arising from transmon-dressed dephasing. Because this dephasing mechanism samples the spectral density at the ancilla–drive detuning (∼GHz), it is relatively insensitive to sideband detuning.

Figure 3(b) displays the simulated gate fidelity as a function of sideband detuning, showing a maximum near 5 MHz. This peak arises from a trade-off between gate speed and decoherence. Qualitatively, the beamsplitter time scales linearly with Δ, while the sideband-dressed decoherence rate follows an approximate Δ^{-2} dependence. As a result, decreasing Δ enhances the interaction rate but more significantly increases decoherence, leading to overall reduced fidelity. Conversely, at large detuning, the dominant decoherence mechanism shifts to photon shot noise arising from transmon-dressed dephasing, which is governed by the transmon–drive detuning (∼ GHz) and thus largely insensitive to MHz-scale variations in Δ. In this regime, further increasing Δ leads to longer gate times without significant improvement in decoherence, again reducing the fidelity. The interplay of these two effects gives rise to the observed fidelity maxi-

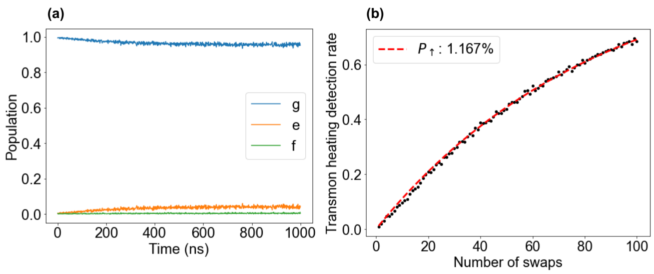

FIG. A5. **Transmon heating during VRBS drive** (a) Transmon population after continuous VRBS drive. (b) Measured the transmon state after each swap gate to detect the transmon heating up to 100 gate operations. We estimate the transmon heating probability as 1.167% per swap gate operation.

mum, which is qualitatively reproduced by the numerical simulations.

Appendix H: Transmon heating detection after each swap operation

Transmon heating events during swap operation prevent coherent oscillation between Alice and Bob, thereby causing dephasing. To detect and characterize these heating events, we measure the transmon state immediately after each swap operation. We perform measurements up to 100 consecutive swap operations, post-selecting out any instances where heating is detected. We fit the transmon heating detection rate $R = 1-(1-P_\uparrow)^n$ to estimate the transmon heating rate per swap operation. Figure A5 illustrates the heating detection rate observed over these 100 swap operations. From these measurements, we estimate a heating probability of approximately 1.167% per swap operation.

Appendix I: Mapping dual-rail cavity states onto transmon states

To measure the populations of single-photon states in the Alice and Bob modes using single-shot readout, we map the cavity states onto the transmon states. The circuit diagram is illustrated in Fig. A6. After reseting the transmon to the ground state, we apply a sideband transition pulse $|g10\rangle \leftrightarrow |f00\rangle$ (corresponding to Alice mode). Subsequently, we apply a photon-number-unselective π_{ef} pulse with a short duration($\Delta t \ll 2\pi/\chi_e^a, 2\pi/\chi_e^b$). Finally, we apply a second sideband transition pulse $|g01\rangle \leftrightarrow |f00\rangle$ (corresponding to Bob mode). Through this sequence, the population in the $|10\rangle$ state maps to the transmon $|e\rangle$ state, the $|01\rangle$ state population maps to $|f\rangle$, and the $|00\rangle$ state maps to $|g\rangle$. This method enables single-shot measurement of $|00\rangle$, $|01\rangle$, $|10\rangle$ states within a duration significantly shorter ($\ll 1/\chi_e$) compared to parity measurement or PNRS, which typically require durations on the order of $1/\chi_e$. The resulting confusion matrix M_{map} for this mapping is

$$M_{\text{map}} = \begin{bmatrix} 0.9959 & 0.0491 & 0.0100 \\ 0.0018 & 0.9467 & 0.0172 \\ 0.0022 & 0.0042 & 0.9728 \end{bmatrix}, \tag{I.1}$$

where the columns correspond prepared states $|00\rangle, |10\rangle$ and $|01\rangle$. The observed asymmetry between Alice and Bob arises from the order of the mapping procedure. We use this confusion matrix to correct readout error originating from the mapping for the beamsplitter operations.

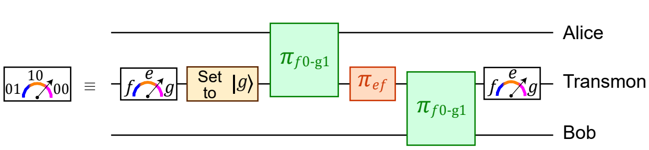

FIG. A6. **Mapping of cavity states to the transmon.** The transmon is first reset to the $|g\rangle$ state by measurement and following conditional π pulse(s). Then a combination of sideband and transmon pulses are applied to perform the mapping: $|00\rangle \to |g\rangle$, $|10\rangle \to |e\rangle$ and $|01\rangle \to |f\rangle$.

Appendix J: Qudit gates

Universal control of a two-qudit system requires the ability to perform arbitrary single-qudit rotations along with at least one entangling operation [82]. In our mul-

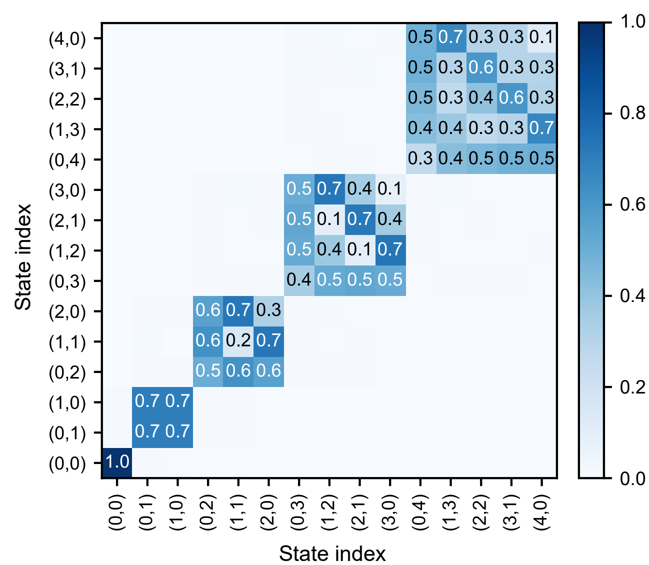

FIG. A7. **Matrix elements of the VRBS operation.** The matrix takes a block-diagonal form when actions on higher Fock states are computed. The simulation is performed with sideband detuning −5.5 MHz. Only amplitudes are shown for brevity.

timode architecture, single-qudit rotations $R_d(\vec{\theta})$ can be implemented using either sideband gates [39] or echoed conditional displacement gates [37]. The VRBS interaction discussed in the main text provides a mechanism for generating entanglement between higher Fock states as well. This operation takes a block-diagonal form, where each basis state $|m, n\rangle$ is rotated within a photon-number-conserving subspace—i.e., among states $|m', n'\rangle$ satisfying $m' + n' = m + n$. Together with single-qudit rotations, this operation enable universal control within a finite-dimensional Hilbert space constructed from d-dimensional qudits. For example, universality in the two-qudit Hilbert space can be performed by:

$$\mathcal{U} = \mathrm{R}_d(\vec{\theta}_0) \otimes \mathrm{R}_d(\vec{\phi}_0) \prod_{i=1}^{N_{\mathrm{block}}} \left[\mathrm{VRBS}\ \mathrm{R}_d(\vec{\theta}_i) \otimes \mathrm{R}_d(\vec{\phi}_i) \right] \tag{J.1}$$

where N_{block} is the number of blocks of those gates within the square brackets.

With the results of Fig. A7, it is possible to investigate the properties of VRBS as a two-qutrit entangling gate, as a concrete example. For qutrits, it has a Schmidt rank of 9. The entangling power, $e_p(U)$ can be defined as the average of the linear entropy over product states $|\Psi\rangle = |\psi\rangle_1 \otimes |\psi_2\rangle$ following [48]:

$$E(|\Psi\rangle) = 1 - \mathrm{Tr}_1 \rho_1^2 \tag{J.2}$$

where $\rho_1 = \mathrm{Tr}_2(U|\Psi\rangle\langle\Psi|U^\dagger)$ is the reduced density matrix, and U is the entangling gate being investigated. We estimate $e_p(\mathrm{VRBS}) = 0.379(2)$ by sampling 10^5 $|\Psi\rangle$, this is similar the standard qutrit CSUM gate ($\mathrm{CSUM}_3|m,n\rangle = |m, m+n \bmod 3\rangle$) which is known analytically to be $e_p(\mathrm{CSUM}_3) = 3/8$ [48]. This implies that VRBS is an efficient qutrit entangling gate. Further, by numerical optimization of the $SU(3)$ angles in Eq. (J.1), approximate synthesis of the CSUM_3 gate from $2 \leq N \leq 6$ blocks were identified with fidelities

$$\mathcal{F}_{\mathrm{CSUM}_3}^{N_{\mathrm{blocks}}} = \{51\%, 88\%, 92\%, 99.1\%, 99.999974\%\} \tag{J.3}$$

Demonstration of universality in our 2-cell system is the topic of future work, with emphasis placed on qudit CSUM gates.

Appendix K: Experimental setup

Figure A8 illustrates the cryogenic wiring diagram of our measurement setup. The microwave components and design choices are carefully optimized to minimize thermal excitation of both the cavity modes and the transmon. The double-cell cavity is mounted vertically within a custom-built support structure—or cage—comprising straight and semicircular clamps made from oxygen-free high thermal conductivity (OFHC) copper, ensuring efficient thermal anchoring and heat extraction.

To suppress infrared (IR) radiation, the cage is wrapped in Eccosorb$^{\mathrm{TM}}$ foam, which absorbs stray IR photons that could otherwise be absorbed by the cavity or surrounding microwave components. Two commercial Eccosorb filters, thermalized via OFHC copper braids, are installed on the drive lines to the cavity and transmon, providing attenuation of high-energy IR photons coming down the coaxial cables. A High-Energy-Radiation-Drain (HERD-2) filter is placed on the readout line to block infrared radiation while minimizing signal attenuation, ensuring high-fidelity readout. All IR filters are mounted inside the Eccosorb-wrapped region for protection against ambient IR photons.

A copper can is mounted on the dilution refrigerator's base plate to enclose and shield all components thermalized to the base (8 mK) temperature. To further reduce susceptibility to magnetic noise, a μ-metal shield is placed around the vacuum chamber, protecting the system from external magnetic fields.

For control and measurement, we use the OPX+ and Octave RF hardware from Quantum Machines. The transmon is read out in reflection via its on-chip readout resonator. A Josephson Parametric Amplifier (JPA) is used as the first-stage phase-insensitive amplifier in the readout chain. The JPA's charge pump (8.375 GHz) and DC bias are supplied by a Rhode&Schwarz SMA100B signal generator and a Yokogawa GS200 DC voltage/current source, respectively.

[1] R. W. Heeres, B. Vlastakis, E. Holland, S. Krastanov, V. V. Albert, L. Frunzio, L. Jiang, and R. J. Schoelkopf, Cavity state manipulation using photon-number selective phase gates, Phys. Rev. Lett. **115**, 137002 (2015).

[2] A. Eickbusch, V. Sivak, A. Z. Ding, S. S. Elder, S. R. Jha, J. Venkatraman, B. Royer, S. M. Girvin, R. J. Schoelkopf, and M. H. Devoret, Fast universal control of an oscillator with weak dispersive coupling to a qubit, Nature Physics **18**, 1464 (2022).

[3] S. Rosenblum, Y. Y. Gao, P. Reinhold, C. Wang, C. J. Axline, L. Frunzio, S. M. Girvin, L. Jiang, M. Mirrahimi, M. H. Devoret, *et al.*, A cnot gate between multiphoton qubits encoded in two cavities, Nature communications **9**, 652 (2018).

[4] R. W. Heeres, P. Reinhold, N. Ofek, L. Frunzio, L. Jiang, M. H. Devoret, and R. J. Schoelkopf, Implementing a universal gate set on a logical qubit encoded in an oscillator, Nature communications **8**, 94 (2017).

[5] Y. Y. Gao, B. J. Lester, K. S. Chou, L. Frunzio, M. H. Devoret, L. Jiang, S. Girvin, and R. J. Schoelkopf, Entanglement of bosonic modes through an engineered exchange interaction, Nature **566**, 509 (2019).

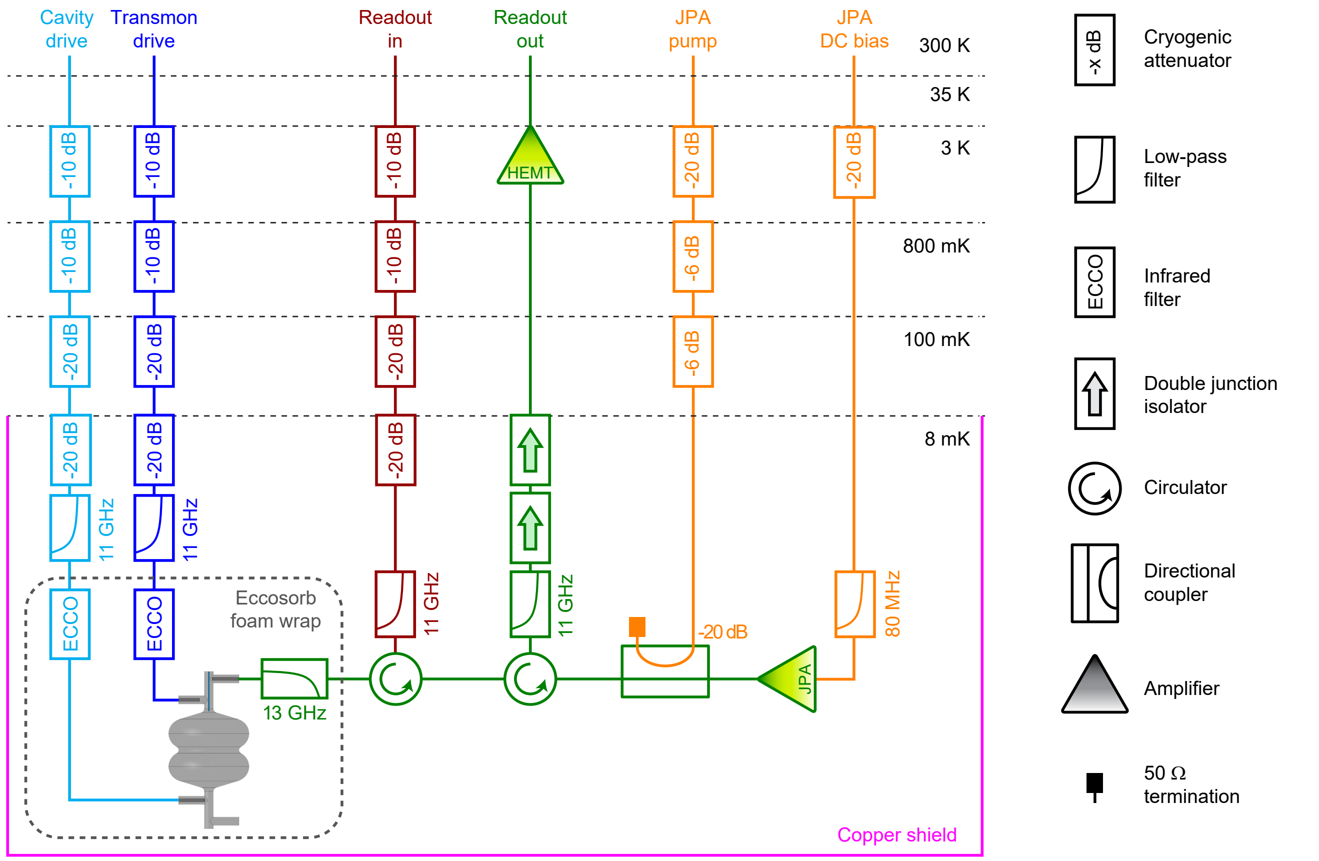

FIG. A8. **Simplified cryogenic wiring diagram.**

[6] B. J. Chapman, S. J. de Graaf, S. H. Xue, Y. Zhang, J. Teoh, J. C. Curtis, T. Tsunoda, A. Eickbusch, A. P. Read, A. Koottandavida, S. O. Mundhada, L. Frunzio, M. Devoret, S. Girvin, and R. Schoelkopf, High-on-off-ratio beam-splitter interaction for gates on bosonically encoded qubits, PRX Quantum **4**, 020355 (2023).

[7] Y. Lu, A. Maiti, J. W. O. Garmon, S. Ganjam, Y. Zhang, J. Claes, L. Frunzio, S. M. Girvin, and R. J. Schoelkopf, High-fidelity parametric beamsplitting with a parity-protected converter, Nature Communications **14**, 5767 (2023).

[8] M. Reagor, W. Pfaff, C. Axline, R. W. Heeres, N. Ofek, K. Sliwa, E. Holland, C. Wang, J. Blumoff, K. Chou, *et al.*, Quantum memory with millisecond coherence in circuit qed, Physical Review B **94**, 014506 (2016).

[9] C. Wang, Y. Y. Gao, P. Reinhold, R. W. Heeres, N. Ofek, K. Chou, C. Axline, M. Reagor, J. Blumoff, K. Sliwa, *et al.*, A schrödinger cat living in two boxes, Science **352**, 1087 (2016).

[10] S. Chakram, A. E. Oriani, R. K. Naik, A. V. Dixit, K. He, A. Agrawal, H. Kwon, and D. I. Schuster, Seamless high-q microwave cavities for multimode circuit quantum electrodynamics, Phys. Rev. Lett. **127**, 107701 (2021).

[11] N. Ofek, A. Petrenko, R. Heeres, P. Reinhold, Z. Leghtas, B. Vlastakis, Y. Liu, L. Frunzio, S. Girvin, L. Jiang, *et al.*, Extending the lifetime of a quantum bit with error correction in superconducting circuits, Nature **536**, 441 (2016).

[12] V. V. Sivak, A. Eickbusch, B. Royer, S. Singh, I. Tsioutsios, S. Ganjam, A. Miano, B. Brock, A. Ding, L. Frunzio, *et al.*, Real-time quantum error correction beyond break-even, Nature **616**, 50 (2023).

[13] Z. Ni, S. Li, X. Deng, Y. Cai, L. Zhang, W. Wang, Z.-B. Yang, H. Yu, F. Yan, S. Liu, *et al.*, Beating the break-even point with a discrete-variable-encoded logical qubit, Nature **616**, 56 (2023).

[14] O. Milul, B. Guttel, U. Goldblatt, S. Hazanov, L. M. Joshi, D. Chausovsky, N. Kahn, E. Çiftyürek, F. Lafont, and S. Rosenblum, Superconducting cavity qubit with tens of milliseconds single-photon coherence time, PRX Quantum **4**, 030336 (2023).

[15] A. E. Oriani, F. Zhao, T. Roy, A. Anferov, K. He, A. Agrawal, R. Banerjee, S. Chakram, and D. I. Schuster, Niobium coaxial cavities with internal quality factors exceeding 1.5 billion for circuit quantum electrodynamics (2024), arXiv:2403.00286 [quant-ph].

[16] A. Romanenko, R. Pilipenko, S. Zorzetti, D. Frolov, M. Awida, S. Belomestnykh, S. Posen, and A. Grassellino, Three-Dimensional Superconducting Resonators at T<20 mK with Photon Lifetimes up to τ=2 s, Phys. Rev. Appl. **13**, 034032 (2020).

[17] M. Mirrahimi, Z. Leghtas, V. V. Albert, S. Touzard, R. J. Schoelkopf, L. Jiang, and M. H. Devoret, Dynamically protected cat-qubits: a new paradigm for universal quantum computation, New Journal of Physics **16**, 045014 (2014).

[18] M. H. Michael, M. Silveri, R. Brierley, V. V. Albert, J. Salmilehto, L. Jiang, and S. M. Girvin, New class of quantum error-correcting codes for a bosonic mode, Physical Review X **6**, 031006 (2016).

[19] B. L. Brock, S. Singh, A. Eickbusch, V. V. Sivak, A. Z. Ding, L. Frunzio, S. M. Girvin, and M. H. Devoret, Quantum error correction of qudits beyond break-even, Nature **641**, 612 (2025).

[20] S. S. Bullock, D. P. O'Leary, and G. K. Brennen, Asymptotically optimal quantum circuits for d-level systems, Phys. Rev. Lett. **94**, 230502 (2005).

[21] G. K. Brennen, D. P. O'Leary, and S. S. Bullock, Criteria for exact qudit universality, Physical Review A—Atomic, Molecular, and Optical Physics **71**, 052318 (2005).

[22] T. de Souza Farias, L. Friedrich, and J. Maziero, A short review on qudit quantum machine learning (2025), arXiv:2505.05158.

[23] Y. Cao, J. Romero, J. P. Olson, M. Degroote, P. D. Johnson, M. Kieferová, I. D. Kivlichan, T. Menke, B. Peropadre, N. P. Sawaya, *et al.*, Quantum chemistry in the age of quantum computing, Chemical reviews **119**, 10856 (2019).

[24] R. Dutta, D. G. A. Cabral, N. Lyu, N. P. Vu, Y. Wang, B. Allen, X. Dan, R. G. Cortiñas, P. Khazaei, M. Schäfer, A. C. C. d. Albornoz, S. E. Smart, S. Nie, M. H. Devoret, D. A. Mazziotti, P. Narang, C. Wang, J. D. Whitfield, A. K. Wilson, H. P. Hendrickson, D. A. Lidar, F. Pérez-Bernal, L. F. Santos, S. Kais, E. Geva, and V. S. Batista, Simulating chemistry on bosonic quantum devices, Journal of Chemical Theory and Computation **20**, 6426 (2024), pMID: 39068594.

[25] Y. Wang, Z. Hu, B. C. Sanders, and S. Kais, Qudits and high-dimensional quantum computing, Frontiers in Physics **8**, 589504 (2020).

[26] Y. Liu, S. Singh, K. C. Smith, E. Crane, J. M. Martyn, A. Eickbusch, A. Schuckert, R. D. Li, J. Sinanan-Singh, M. B. Soley, T. Tsunoda, I. L. Chuang, N. Wiebe, and S. M. Girvin, Hybrid oscillator-qubit quantum processors: Instruction set architectures, abstract machine models, and applications (2024), arXiv:2407.10381 [quant-ph].

[27] E. J. Gustafson, H. Lamm, F. Lovelace, and D. Musk, Primitive quantum gates for an SU(2) discrete subgroup: Binary tetrahedral, Phys. Rev. D **106**, 114501 (2022), arXiv:2208.12309 [quant-ph].

[28] J. Huang, T. J. DiNapoli, G. Rockwood, M. Yuan, P. Narasimhan, E. Gupta, M. Bal, F. Crisa, S. Garattoni, Y. Lu, L. Jiang, and S. Chakram, Fast sideband control of a weakly coupled multimode bosonic memory, arXiv preprint arXiv:2503.10623 (2025).

[29] X. You, A. C. Y. Li, T. Roy, S. Zhu, A. Romanenko, A. Grassellino, Y. Lu, and S. Chakram, Floquet-Engineered Fast SNAP gates with optimal control in weakly coupled cQED systems (2025), in preparation.

[30] I. Pietikäinen, O. Černotík, A. Eickbusch, A. Maiti, J. W. Garmon, R. Filip, and S. M. Girvin, Strategies and tradeoffs for controllability and memory time of ultra-high-quality microwave cavities in circuit quantum electrodynamics, PRX Quantum **5**, 040307 (2024).

[31] B. Aune, R. Bandelmann, D. Bloess, B. Bonin, A. Bosotti, M. Champion, C. Crawford, G. Deppe, B. Dwersteg, D. A. Edwards, H. T. Edwards, M. Ferrario, M. Fouaidy, P.-D. Gall, A. Gamp, A. Gössel, J. Graber, D. Hubert, M. Hüning, M. Juillard, T. Junquera, H. Kaiser, G. Kreps, M. Kuchnir, R. Lange, M. Leenen, M. Liepe, L. Lilje, A. Matheisen, W.-D. Möller, A. Mosnier, H. Padamsee, C. Pagani, M. Pekeler, H.-B. Peters, O. Peters, D. Proch, K. Rehlich, D. Reschke, H. Safa, T. Schilcher, P. Schmüser, J. Sekutowicz, S. Simrock, W. Singer, M. Tigner, D. Trines, K. Twarowski, G. Weichert, J. Weisend, J. Wojtkiewicz, S. Wolff, and K. Zapfe, Superconducting tesla cavities, Phys. Rev. ST Accel. Beams **3**, 092001 (2000).

[32] A. Reineri, S. Zorzetti, T. Roy, and X. You, Exploration of superconducting multi-mode cavity architectures for quantum computing, in *2023 IEEE International Conference on Quantum Computing and Engineering (QCE)*, Vol. 01 (2023) pp. 1342–1348.

[33] T. Roy, T. Kim, A. Romanenko, and A. Grassellino, Qudit-based quantum computing with SRF cavities at Fermilab, PoS **LATTICE2023**, 127 (2024).

[34] S. Krastanov, V. V. Albert, C. Shen, C.-L. Zou, R. W. Heeres, B. Vlastakis, R. J. Schoelkopf, and L. Jiang, Universal control of an oscillator with dispersive coupling to a qubit, Phys. Rev. A **92**, 040303 (2015).

[35] A. Eickbusch, V. Sivak, A. Z. Ding, S. S. Elder, S. R. Jha, J. Venkatraman, B. Royer, S. M. Girvin, R. J. Schoelkopf, and M. H. Devoret, Fast universal control of an oscillator with weak dispersive coupling to a qubit, Nature Physics **18**, 1464 (2022).

[36] A. A. Diringer, E. Blumenthal, A. Grinberg, L. Jiang, and S. Hacohen-Gourgy, Conditional-not displacement: Fast multioscillator control with a single qubit, Phys. Rev. X **14**, 011055 (2024).

[37] X. You, Y. Lu, T. Kim, D. M. Kürkçüolu, S. Zhu, D. van Zanten, T. Roy, Y. Lu, S. Chakram, A. Grassellino, A. Romanenko, J. Koch, and S. Zorzetti, Crosstalk-robust quantum control in multimode bosonic systems, Phys. Rev. Appl. **22**, 044072 (2024).

[38] S. Zeytinoğlu, M. Pechal, S. Berger, A. A. Abdumalikov, A. Wallraff, and S. Filipp, Microwave-induced amplitude- and phase-tunable qubit-resonator coupling in circuit quantum electrodynamics, Phys. Rev. A **91**, 043846 (2015).

[39] Y. Liu, J. Sinanan-Singh, M. T. Kearney, G. Mintzer, and I. L. Chuang, Constructing qudits from infinite-dimensional oscillators by coupling to qubits, Phys. Rev. A **104**, 032605 (2021).

[40] C. K. Law and J. H. Eberly, Arbitrary control of a quantum electromagnetic field, Physical review letters **76**, 1055 (1996).

[41] S. Rosenblum, P. Reinhold, M. Mirrahimi, L. Jiang, L. Frunzio, and R. J. Schoelkopf, Fault-tolerant detection of a quantum error, Science **361**, 266–270 (2018).

[42] S. S. Elder, C. S. Wang, P. Reinhold, C. T. Hann, K. S. Chou, B. J. Lester, S. Rosenblum, L. Frunzio, L. Jiang, and R. J. Schoelkopf, High-fidelity measurement of qubits encoded in multilevel superconducting circuits, Phys. Rev. X **10**, 011001 (2020).

[43] P. Reinhold, S. Rosenblum, W.-L. Ma, L. Frunzio, L. Jiang, and R. J. Schoelkopf, Error-corrected gates on an encoded qubit, Nature Physics **16**, 822–826 (2020).

[44] T. Tsunoda, J. D. Teoh, W. D. Kalfus, S. J. de Graaf, B. J. Chapman, J. C. Curtis, N. Thakur, S. M. Girvin, and R. J. Schoelkopf, Error-detectable bosonic entangling gates with a noisy ancilla, PRX Quantum **4**, 020354 (2023).

[45] J. D. Teoh, P. Winkel, H. K. Babla, B. J. Chapman,

J. Claes, S. J. de Graaf, J. W. Garmon, W. D. Kalfus, Y. Lu, A. Maiti, *et al.*, Dual-rail encoding with superconducting cavities, Proceedings of the National Academy of Sciences **120**, e2221736120 (2023).
[46] M. Hofheinz, H. Wang, M. Ansmann, R. C. Bialczak, E. Lucero, M. Neeley, A. O'connell, D. Sank, J. Wenner, J. M. Martinis, *et al.*, Synthesizing arbitrary quantum states in a superconducting resonator, Nature **459**, 546 (2009).
[47] B. Mischuck and K. Mølmer, Qudit quantum computation in the jaynes-cummings model, Phys. Rev. A **87**, 022341 (2013).
[48] X. Wang, B. C. Sanders, and D. W. Berry, Entangling power and operator entanglement in qudit systems, Phys. Rev. A **67**, 042323 (2003).
[49] E. O. Kiktenko, A. S. Nikolaeva, P. Xu, G. V. Shlyapnikov, and A. K. Fedorov, Scalable quantum computing with qudits on a graph, Phys. Rev. A **101**, 022304 (2020).
[50] A. S. Nikolaeva, E. O. Kiktenko, and A. K. Fedorov, Efficient realization of quantum algorithms with qudits, EPJ Quant. Technol. **11**, 43 (2024), arXiv:2111.04384 [quant-ph].
[51] A. S. Nikolaeva, E. O. Kiktenko, and A. K. Fedorov, Generalized Toffoli Gate Decomposition Using Ququints: Towards Realizing Grover's Algorithm with Qudits, Entropy **25**, 387 (2023), arXiv:2212.12505 [quant-ph].
[52] A. S. Nikolaeva *et al.*, Scalable improvement of the generalized Toffoli gate realization using trapped-ion-based qutrits (2024), arXiv:2407.07758 [quant-ph].
[53] E. J. Gustafson, H. Lamm, D. Liu, E. M. Murairi, and S. Zhu, Synthesis of Single Qutrit Circuits from Clifford+R (2025), arXiv:2503.20203 [quant-ph].
[54] A. Agrawal, A. V. Dixit, T. Roy, S. Chakram, K. He, R. K. Naik, D. I. Schuster, and A. Chou, Stimulated emission of signal photons from dark matter waves, Phys. Rev. Lett. **132**, 140801 (2024).
[55] X. Deng, S. Li, Z.-J. Chen, Z. Ni, Y. Cai, J. Mai, L. Zhang, P. Zheng, H. Yu, C.-L. Zou, *et al.*, Quantum-enhanced metrology with large fock states, Nature Physics , 1 (2024).
[56] E. Gustafson, Prospects for Simulating a Qudit Based Model of (1+1)d Scalar QED, Phys. Rev. D **103**, 114505 (2021), arXiv:2104.10136 [quant-ph].
[57] A. Ciavarella, N. Klco, and M. J. Savage, Trailhead for quantum simulation of SU(3) Yang-Mills lattice gauge theory in the local multiplet basis, Phys. Rev. D **103**, 094501 (2021), arXiv:2101.10227 [quant-ph].
[58] T. V. Zache, D. González-Cuadra, and P. Zoller, Fermion-qudit quantum processors for simulating lattice gauge theories with matter, Quantum **7**, 1140 (2023), arXiv:2303.08683 [quant-ph].
[59] C. W. Bauer, Z. Davoudi, A. B. Balantekin, T. Bhattacharya, M. Carena, W. A. De Jong, P. Draper, A. El-Khadra, N. Gemelke, M. Hanada, *et al.*, Quantum simulation for high-energy physics, PRX quantum **4**, 027001 (2023).
[60] M. Illa, C. E. P. Robin, and M. J. Savage, Quantum simulations of SO(5) many-fermion systems using qudits, Phys. Rev. C **108**, 064306 (2023), arXiv:2305.11941 [quant-ph].
[61] D. M. Kürkçüoglu, H. Lamm, and A. Maestri, Qudit Gate Decomposition Dependence for Lattice Gauge Theories (2024), arXiv:2410.16414 [quant-ph].
[62] Y. Y. Gao, B. J. Lester, Y. Zhang, C. Wang, S. Rosenblum, L. Frunzio, L. Jiang, S. M. Girvin, and R. J. Schoelkopf, Programmable interference between two microwave quantum memories, Phys. Rev. X **8**, 021073 (2018).
[63] W. Pfaff, C. J. Axline, L. D. Burkhart, U. Vool, P. Reinhold, L. Frunzio, L. Jiang, M. H. Devoret, and R. J. Schoelkopf, Controlled release of multiphoton quantum states from a microwave cavity memory, Nature Physics **13**, 882 (2017).
[64] M. Boissonneault, J. M. Gambetta, and A. Blais, Improved qubit bifurcation readout in the straddling regime of circuit qed, Phys. Rev. A **86**, 022326 (2012).
[65] Y. Zhang, B. J. Lester, Y. Y. Gao, L. Jiang, R. J. Schoelkopf, and S. M. Girvin, Engineering bilinear mode coupling in circuit QED: Theory and experiment, Phys. Rev. A **99**, 012314 (2019).
[66] K. S. Chou, T. Shemma, H. McCarrick, T.-C. Chien, J. D. Teoh, P. Winkel, A. Anderson, J. Chen, J. C. Curtis, S. J. de Graaf, *et al.*, A superconducting dual-rail cavity qubit with erasure-detected logical measurements, Nature Physics **20**, 1454 (2024).
[67] Z. Li, E. Gupta, F. Zhao, R. Banerjee, Y. Lu, T. Roy, A. Oriani, A. Vrajitoarea, S. Chakram, and D. I. Schuster, A cascaded random access quantum memory, arXiv preprint arXiv:2503.13953 (2025).
[68] C. Zhou, P. Lu, M. Praquin, T.-C. Chien, R. Kaufman, X. Cao, M. Xia, R. S. Mong, W. Pfaff, D. Pekker, *et al.*, Realizing all-to-all couplings among detachable quantum modules using a microwave quantum state router, npj quantum information **9**, 54 (2023).
[69] A. Blais, A. L. Grimsmo, S. M. Girvin, and A. Wallraff, Circuit quantum electrodynamics, Rev. Mod. Phys. **93**, 025005 (2021).
[70] F. Yan, S. Gustavsson, J. Bylander, X. Jin, F. Yoshihara, D. G. Cory, Y. Nakamura, T. P. Orlando, and W. D. Oliver, Rotating-frame relaxation as a noise spectrum analyser of a superconducting qubit undergoing driven evolution, Nature Communications **4**, 10.1038/ncomms3337 (2013).
[71] A. A. Clerk and D. W. Utami, Using a qubit to measure photon-number statistics of a driven thermal oscillator, Phys. Rev. A **75**, 042302 (2007).
[72] Z. Wang, S. Shankar, Z. Minev, P. Campagne-Ibarcq, A. Narla, and M. Devoret, Cavity attenuators for superconducting qubits, Phys. Rev. Appl. **11**, 014031 (2019).
[73] A. P. Read, B. J. Chapman, C. U. Lei, J. C. Curtis, S. Ganjam, L. Krayzman, L. Frunzio, and R. J. Schoelkopf, Precision measurement of the microwave dielectric loss of sapphire in the quantum regime with parts-per-billion sensitivity, Phys. Rev. Appl. **19**, 034064 (2023).
[74] S. Posen, A. Romanenko, A. Grassellino, O. Melnychuk, and D. Sergatskov, Ultralow surface resistance via vacuum heat treatment of superconducting radio-frequency cavities, Phys. Rev. Appl. **13**, 014024 (2020).
[75] A. Romanenko and D. I. Schuster, Understanding quality factor degradation in superconducting niobium cavities at low microwave field amplitudes, Phys. Rev. Lett. **119**, 264801 (2017).
[76] S. Ganjam, Y. Wang, Y. Lu, A. Banerjee, C. U. Lei, L. Krayzman, K. Kisslinger, C. Zhou, R. Li, Y. Jia, M. Liu, L. Frunzio, and R. J. Schoelkopf, Surpassing millisecond coherence in on chip superconducting quantum memories by optimizing materials and circuit design, Na-

ture Communications **15**, 3687 (2024).

[77] H. Breuer and F. Petruccione, *The Theory Of Open Quantum Systems* (Oxford University Press, 2002) Chap. 3.

[78] J. Li, M. A. Sillanpää, G. S. Paraoanu, and P. J. Hakonen, Pure dephasing in a superconducting three-level system, Journal of Physics: Conference Series **400**, 042039 (2012).

[79] J. Koch, T. M. Yu, J. Gambetta, A. A. Houck, D. I. Schuster, J. Majer, A. Blais, M. H. Devoret, S. M. Girvin, and R. J. Schoelkopf, Charge-insensitive qubit design derived from the cooper pair box, Phys. Rev. A **76**, 042319 (2007).

[80] P. Groszkowski, A. D. Paolo, A. L. Grimsmo, A. Blais, D. I. Schuster, A. A. Houck, and J. Koch, Coherence properties of the 0-π qubit, New Journal of Physics **20**, 043053 (2018).

[81] I. Shavitt and L. T. Redmon, Quasidegenerate perturbation theories. a canonical van Vleck formalism and its relationship to other approaches, The Journal of Chemical Physics **73**, 5711 (1980).

[82] S. L. Braunstein and P. van Loock, Quantum information with continuous variables, Rev. Mod. Phys. **77**, 513 (2005).